END

FILMED

DTIC

AD-A161 731

DNA-TR-84-170

DEVELOPMENT AND TESTING OF AN OPTICAL EXTINCTION PROBE FOR MEASURING LOFTED DUST FLOW DENSITIES

M.B. Petach
C.M. Dube
D.T. Hove
Dynamics Technology, Inc.
22939 Hawthorne Boulevard
Torrance, CA 90505-3693

16 April 1984

Technical Report

CONTRACT No. DNA 001-83-C-0403

Approved for public release;
distribution is unlimited.

DTIC FILE COPY

Prepared for
   Director
   DEFENSE NUCLEAR AGENCY
   Washington, DC 20305-1000

DTIC
ELECTE
NOV 1 4 1985
B

85 7 30 034

AD-A161731

REPORT DOCUMENTATION PAGE

1a REPORT SECURITY CLASSIFICATION	1b RESTRICTIVE MARKINGS
UNCLASSIFIED	

2a SECURITY CLASSIFICATION AUTHORITY	3 DISTRIBUTION / AVAILABILITY OF REPORT
	Approved for public release;
2b DECLASSIFICATION DOWNGRADING SCHEDULE N/A since UNCLASSIFIED	distribution is unlimited.

4 PERFORMING ORGANIZATION REPORT NUMBER(S)	5 MONITORING ORGANIZATION REPORT NUMBER(S)
	DNA-TR-84-170

6a NAME OF PERFORMING ORGANIZATION	6b OFFICE SYMBOL (If applicable)	7a NAME OF MONITORING ORGANIZATION
Dynamics Technology, Inc		Director Defense Nuclear Agency

6c. ADDRESS (City, State, and ZIP Code)	7b ADDRESS (City, State, and ZIP Code)
22939 Hawthorne Boulevard Torrance, CA 90505-3693	Washington, DC 20305-1000

8a NAME OF FUNDING / SPONSORING ORGANIZATION	8b OFFICE SYMBOL (If applicable)	9 PROCUREMENT INSTRUMENT IDENTIFICATION NUMBER
		DNA 001-83-C-0403

8c. ADDRESS (City, State, and ZIP Code)	10 SOURCE OF FUNDING NUMBERS			
	PROGRAM ELEMENT NO 62715H	PROJECT NO C99QMXW	TASK NO A	WORK UNIT ACCESSION NO DH007339

11 TITLE (Include Security Classification)

DEVELOPMENT AND TESTING OF AN OPTICAL EXTINCTION PROBE FOR MEASURING LOFTED DUST FLOW DENSITIES

12 PERSONAL AUTHOR(S)
M. B. Petach, C. M. Dube, D. T. Hove

13a TYPE OF REPORT	13b TIME COVERED	14 DATE OF REPORT (Year Month Day)	15 PAGE COUNT
Technical Report	FROM 830701 TO 840228	1984, April 16	92

16 SUPPLEMENTARY NOTATION
This work was sponsored by the Defense Nuclear Agency under RDT&E RMSS Code B310084466 C99QMXWA00003 H2590D.

17	COSATI CODES		18 SUBJECT TERMS (Continue on reverse if necessary and identify by block number)	
FIELD	GROUP	SUB-GROUP	Airblast	Dust Lofting
19	4		Dust Probe	Optical Extinction
17	8		Fiber Optics	

19 ABSTRACT (Continue on reverse if necessary and identify by block number)

An optical extinction probe for measuring the mass concentration of dust lofted in high explosive field tests and shock tube experiments was designed and tested. Low cost optical components provide the necessary optical dynamic range for measuring mass concentrations from 10^{-4} to 10^{-2} gm/cm^3. Fiber optics carry the light signal to the measurement points so that the electro-optics can be placed out of the blast environment. Tests using a laboratory version of the probe and representative dust samples demonstrated that the probe could make repeatable measurements in the range of 10^{-4} to 10^{-2} gm/cm^3. Laboratory tests also demonstrated that the measurement range could be varied by changing the optical path length.

Information obtained from an independent service laboratory confirmed that the probe calibration curves scaled to the particle size distribution of the different dust samples as expected. However, predictions of dust mass concentration based on the particle size distribution information differed from measurements made in the calibration tests by up to 75%.

20 DISTRIBUTION / AVAILABILITY OF ABSTRACT	21 ABSTRACT SECURITY CLASSIFICATION
☐ UNCLASSIFIED/UNLIMITED ☒ SAME AS RPT ☐ DTIC USERS	UNCLASSIFIED

22a NAME OF RESPONSIBLE INDIVIDUAL	22b TELEPHONE (Include Area Code)	22c OFFICE SYMBOL
Betty L. Fox	(202) 325-7042	DNA/STTI

DD FORM 1473, 84 MAR

83 APR edition may be used until exhausted
All other editions are obsolete

SECURITY CLASSIFICATION OF THIS PAGE

19. ABSTRACT (Continued)

Based on the findings of this program it is recommended that the optical probe be characterized by direct calibration rather than calculated from particle size distribution information.

A prototype measurement station was designed to withstand ideal and precursed shocks with peak overpressures up to 100 psi. This preliminary design allows measurements to be made at six heights above the ground ($\frac{1}{2}$", 2", $3\frac{1}{2}$", 5", and 8").

SUMMARY

Dynamics Technology's development program has resulted in the construction and testing of a laboratory prototype optical probe which provides a measure of the mass concentration of airborne dust in the range of 10^{-4} to 10^{-2} gm/cm^3 ($\rho_{dust}/\rho_{air} \sim 0.1$ to 10). The probe uses an infrared LED light source and a silicon photodiode to measure the attenuation of light passing through the dust. Optical fibers carry the light to the measurement points. The use of inexpensive LEDs, fibers, couplers and photodiodes allows a low cost per spatial measurement point, and the use of optical fibers allows delicate electronics and most optical components to be housed in a remote location. The probe provides a pulsed optical signal allowing spurious ambient light and electronics zero-drift to be measured and accounted for.

The prototype probe was calibrated over a range of dust densities similar to those measured in the Pre-Direct Course event, using both commercially available graded sand and a representative dust sample from the Direct Course test bed. Experiments demonstrated that the range of dust densities measured can be varied by changing the optical path length. In addition, the particle density and size distribution of the graded sand and the dust sample from the Pre-Direct Course test bed were measured by an independent service laboratory, and the results were used as a basis for making a priori estimates of the optical attenuation versus dust density.

A measurement station to house the optical probes in high explosive field tests and in shock tube tests was designed. The measurement station was sized to minimize aerodynamic interference and to withstand expected shock conditions. A digital data acquisition system for the probes was designed for use during high explosive field tests, as was an underground vault for containing the probe electronics, the optical emitters and detectors, and the data acquisition system.

PREFACE

This program was conducted for the Defense Nuclear Agency under contract DNA-000-83-C-0403 to develop the design for a fiber optic dust probe. The effort was funded under the Small Business Innovative Research Program and was performed from July 1983 to February 1984. Dr. Paul R. Rohr was the technical monitor.

The Dynamics Technology, Inc. Program Manager was Duane Hove. Michael Petach assembled the test equipment, conducted the development tests and prepared the final designs. Dr. C. Michael Dube provided valuable technical guidance.

This work has undergone an extensive internal review before release, both for technical and non-technical content, by an independent review committee.
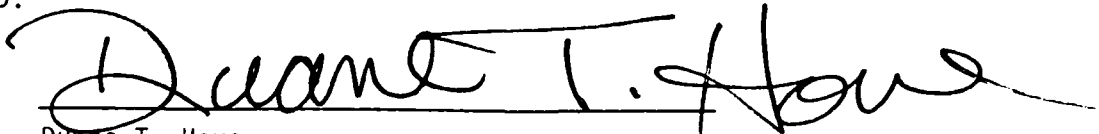
APPROVED:

_____

C. M. Dube

APPROVED:

_____

Duane T. Hove

TABLE OF CONTENTS

iii

LIST OF ILLUSTRATIONS

LIST OF ILLUSTRATIONS (Continued)

LIST OF TABLES

SECTION 1. INTRODUCTION

Dynamics Technology has conducted a program to develop a low cost instrument for measuring airborne dust densities. The dust diagnostic technique measures the attenuation of a light beam across a short pathlength through the dust. A light source coupled to an optical fiber transmits the beam to the measurement point, then another fiber returns the attenuated signal to a photodetector.

1.1 Objectives

The overall objective of this program was to develop a rugged inexpensive optical probe to provide spatial (multiple probe heights and probe locations) and temporal measurements of airborne dust lofted during nuclear blast wave simulations. Specifically, there were two major technical objectives. First, suitable components were to be selected through a laboratory evaluation program, assembled as a laboratory version of the probe, and tested to determine measurement range and accuracy. Second, a preliminary design of a prototype measurement station to house the probes was to be prepared, and a data acquisition system for field tests was to be specified.

1.2 Background

During tests in the 1950's it was observed that large quantities of dust were lofted by the blast waves from nuclear bursts. Extensive efforts were made to quantify the effects of dust on the blast flowfield because of the observed enhanced damage to target structures. Interest in blast wave lofted dust continued because it was found to (1) enhance the airblast induced dynamic pressure; (2) influence the design of air entrainment systems for hardened shelters; (3) obscure ground based radar and optical sensors; and (4) act as the source of dust for nonsurface burst dust clouds, which can interfere with airborne operations.

In order to quantify these effects, physical measurements of the lofted dust from high explosive tests are required to provide inputs to the dust lofting models and to check the ability of predictive codes to calculate the dust

1

transport. Such measurements are difficult and the instruments are often expensive because of the high overpressures of interest (tens of atmospheres), the short durations of the events (tens to hundreds of milliseconds), and the high dust masses involved (order of the air density).

Many techniques have been considered to measure the dust raised by the shock wave during a nuclear blast simulation. Electromagnetic propagation, ionizing radiation, sound speed, pitot probe and capacitance gage techniques were critically reviewed by Hartenbaum.[1] Additional suggestions for optical extinction, holography, microwave and x-ray measurements have been made by various investigators.

The Defense Nuclear Agency conducted non-nuclear burst tests in 1971 (Middle Gust II) and in 1982 and 1983 (Direct Course series) employing several dust diagnostic techniques. The various dust diagnostic techniques displayed varying degrees of success, but none provided a definitive spatial and temporal history of the dust flow. Two optical extinction dust measurement systems were fielded in the Pre Direct Course event; a laser diode-based optical absorption instrument,[2] and a HeNe laser based optical absorption and scattering system.[3] The laser diode system survived the blast and provided a continuous history of the dust flow past a single point; the HeNe laser system only provided an incomplete record because higher than expected shock overpressures caused optical misalignment. Thus, the viability of optical extinction dust diagnostic techniques was demonstrated, but the need for a rugged system was also clearly indicated. Although the laser diode-system was successful, it had three drawbacks. First, there was only one spatial measurement point. Second, the measurement point was between two blast wings such that there is a good possibility that the measured flow was disturbed. Third, this data was reduced assuming a linear relationship between light extinction and dust density rather than the actual exponential relationship. So far, no single approach has proven completely satisfactory.

SECTION 2. THEORY

Mass concentration of airborne dust can be determined by measuring the atten-
uation of a light beam that passes through the dust. Desired ranges of mass
concentrations are selected by varying the optical path length through the
dust.

2.1 Optical Transmission Through Airborne Dust

The transmission of light through a homogeneous dispersion of uniform diameter
spherical particles which both scatter and absorb light is given by the
Bouguer-Beer-Lambert law:

$$T = \frac{I}{I_0} = \exp\left(-\frac{3}{2}\frac{Q}{\rho d}C\ell\right) \qquad (1)$$

where T = transmission ratio

   I = intensity of received light

   I_0 = intensity of received light when no particles are present

   Q = dimensionless extinction factor which accounts for
        both absorption and scattering losses

   ρ = particle density

   d = particle diameter

   C = mass concentration of particles

   ℓ = optical path length through the particles

Real lofted dust flows have a distribution of particle sizes rather than a
uniform particle size. The Bouguer-Beer-Lambert law can be applied to a
polydispersion of spherical particles in the form given by Dobbins[4]

$$T = \frac{I}{I_0} = \exp\left(-\frac{3}{2}\frac{\bar{Q}}{\rho d_{32}}C\ell\right) \qquad (2)$$

3

where $\bar{Q}$ = average extinction factor = $\Sigma(NQ\bar{d}^2\Delta)/\Sigma(N\bar{d}^2\Delta)$ (3)

d_{32} = volume-to-surface mean particle diameter =   (4)
$\Sigma(N\bar{d}^3\Delta)/\Sigma(N\bar{d}^2\Delta) = \Sigma(\chi\Delta)/(\chi\Delta/\bar{d})$

and Δ = particle size interval

$\bar{d}$ = midpoint of the interval Δ

N = number of particles per interval Δ

χ = % of the total weight in the interval Δ

The mass concentration as a function of received intensity is found by solving equation (2) for C, yielding

$$C = (-\frac{3}{2}\frac{\bar{Q}}{\rho d_{32}}\ell)^{-1}\ \ell n\ (\frac{I}{I_o})$$ (5)

Then for a particle distribution characterized by the term $\dfrac{\bar{Q}}{\rho d_{32}}$ the range of mass concentrations determined by a given range of optical transmissions can be varied by changing the interrogating path length (Figure 2.1).
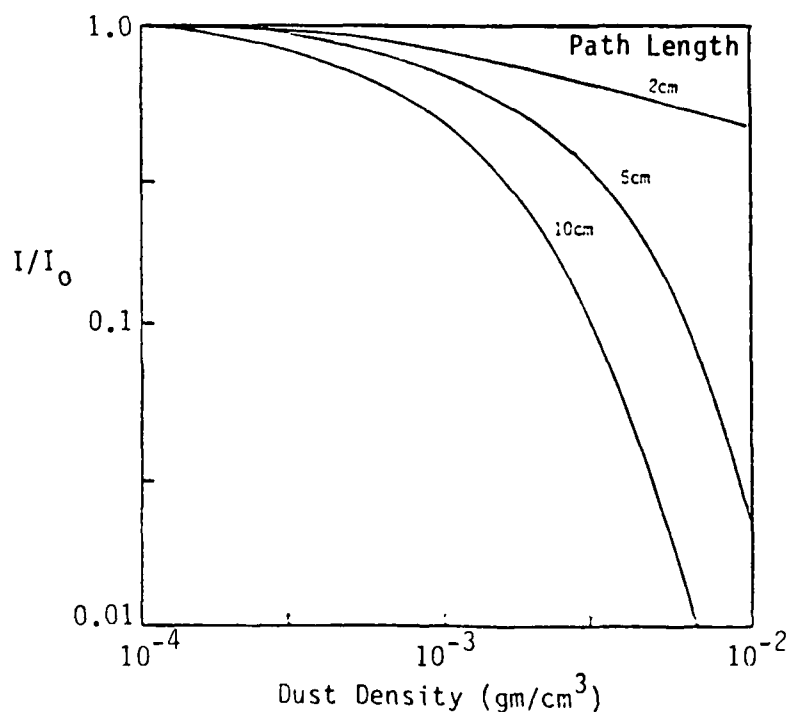
Figure 2.1   Example of the Effect of Path Length on the Range of Dust Densities Measured by a Given Range of Transmissions

4

Once the term $\dfrac{\bar{Q}}{\rho d_{32}}$ is known, the transmission of light across an optical path length ℓ provides a measure of dust mass concentration. The term $\dfrac{\bar{Q}}{\rho d_{32}}$ is a function of both the particle size distribution and of the optical character-istics of the interrogating instrument. Obviously, the particle size distri-bution affects both $\bar{Q}$ and d_{32}, as shown by equations (3) and (4). In addi-tion, the optical characteristics of the interrogating instrument also affect the term $\bar{Q}$ in equation (3). For particle diameters larger than the optical wavelength λ (in the application of interest, $d \gg \lambda$), the value of Q asymp-totically approaches a value of 2 if no scattered light strikes the detector. But $\bar{Q} = 2$ only if the interrogating beam is perfectly collimated and an ideal far field detector is used. In real devices the finite aperture of the detec-tor allows some of the scattered light to be measured, particularly from large particles which scatter strongly in the forward direction, so $\bar{Q}$ may be less than 2. Furthermore, real dust particles are not spherical, so equation (2) does not hold exactly.

There are several methods of determining an optical probe's characteristic transmission vs. dust mass concentration curve for a given particle distribu-tion. The most direct method is to experimentally determine the term $\dfrac{\bar{Q}}{\rho d_{32}}$ through a calibration in which I/I_0 vs. C is measured using a representative dust sample. Another method is to experimentally determine d_{32} and ρ from a representative dust sample, and assume a value of $\bar{Q}$ (typically $\bar{Q} \approx 2$ for large particles). Both of these methods were assessed in the present program.

An alternative approach to probe characterization is to assume a value of $\bar{Q}$, measure ρ from a representative soil sample, and then estimate d_{32} from real time optical scattering measurements made during the event. This method does not depend on a representative sample distribution so it has the potential for being more accurate. However, it is very difficult to implement, as will be discussed in the next section.

2.2 In-Situ Particle Sizing Considerations

In-situ particle sizing can be accomplished by measuring the angular dependence of the relative intensity of forward scattered light. This is possible because forward scattering intensity from a particle of diameter d peaks at a characteristic angle of $0.438 \frac{\lambda}{d}$ rad. For example, if near infrared light of λ = 820 nm is used, the characteristic scattering angles for particles in the size range of interest are given in Table 2.1.

Table 2.1 Principal Scattering Angles for Dust Particles

PARTICLE DIAMETER d (microns)	SCATTERING ANGLE θ (degrees)
10	2.1
25	0.82
50	0.41
75	0.27
100	0.21
200	0.11

If a photodetector array located an appropriate distance (the order of 10 cm) from the scattering volume is used to size 10 μ to 100 μ particles into 4 ranges, then detectors would need to be placed at 0.36 cm, .14 cm, .072 cm, .048 cm and .036 cm from the beam axis. Obviously, the physical size of commercially available photodetectors makes this impractical. In addition, the scattered light power levels are approximately 20 dB down from the direct beam. Wuerker[2] has investigated an approach to scattering measurements which could be adapted to the probe configuration developed in this program. Wuerker's system is based on the fact that all light entering a lens at a given angle is brought to a common focal point in the focal plane. Thus, the conical scattering at an angle ϕ is transformed by a lens of focal length f into a ring of radius $s = f \tan(\phi)$ in the focal plane of the lens. If the

focal plane is divided into annular regions, the intensity in each zone is proportional to the number of particles in the size range with the corresponding conical scattering angle, and also to the cross sectional area of the particles. However, the radii s of interest for practical systems are still the order of a millimeter or less. Calculations in Appendix C indicate the structural vibration from shock loading could result in deflections that preclude useful size distribution estimates.

2.3 Sensitivity Analysis

The relative error in calculating the mass concentration C from optical transmissions is

$$\frac{dC}{C} = \left[\left(\frac{d\rho}{\rho}\right)^2 + \left(\frac{d\ d_{32}}{d_{32}}\right) + \left(\frac{d\ell}{\ell}\right) + \left(\frac{d\bar{Q}}{\bar{Q}}\right)^2 + \left(\frac{dI}{I}\right)^2 \left(\ell n\ \frac{I}{I_o}\right)^{-2} \right]^{-1/2} \quad (6)$$

Thus, the relative error in C is directly proportional to the relative error in ρ, d_{32}, ℓ and $\bar{Q}$. However, the relative error is a nonlinear function of intensity. This term can be examined by plotting lines of constant measurement accuracy $\frac{dC}{C}$ versus $\frac{I}{I_o}$ and $\frac{dI}{I_o}$ (Figure 2.2).

This figure shows, for example, that if a sensor has 1% transmission resolution, then dust concentration measurements with 10% accuracy are limited to transmissions ranging from 90% to 3%. Or, if a sensor measures transmissions down to I/I_o = 1%, dust concentration measurements with 10% accuracy require at least a 1/2% transmission resolution.
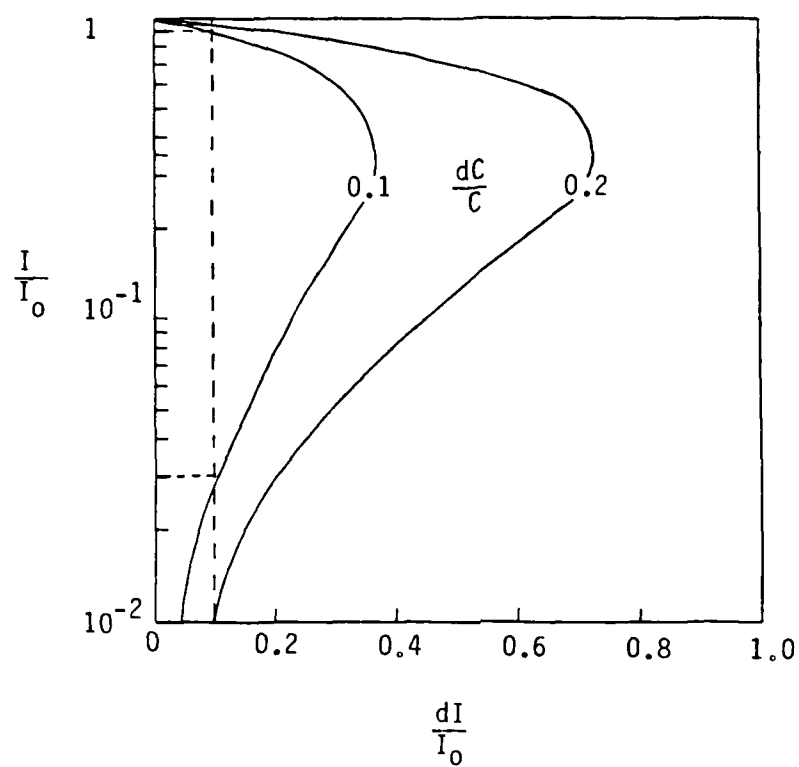
Figure 2.2 Relative Error in Mass Concentration as a Function
of I/I_0 and dI/I_0

SECTION 3. PROBE DEVELOPMENT AND EVALUATION PROGRAM

In addition to cost considerations, two major design issues were addressed. First, the emitter optical power, system power losses and detector sensitivity must provide sufficient dust density dynamic range. Second, the system must physically fit into the proposed measurement station. The power issue affected every component in the system; the problem of fitting the probe into the measurement station mainly affected the collimation and focusing optics.

3.1 Design Considerations

The primary design criterion was that the probe had to measure the expected range of dust mass concentrations with a reasonable degree of accuracy. Data from the Pre-Direct Course event provided an estimate for the expected range of dust densities.

For example, Wisotski's[3] laser-diode attenuation data shows (once the dust density is calculated on an exponential scale) that normalized dust mass concentrations from $\rho_{dust}/\rho_{air} = 0.3$ to $\rho_{dust}/\rho_{air} = 9$ were observed at a six inch height above a finished dusty surface 205 feet from ground zero (Figure 3.1). Dust densities decrease with distance above the ground, and depend on the distance from ground zero, so a nominal design range of $C = 10^{-4}$ to 10^{-2} g/cc was chosen. The optical requirements then can be estimated following the discussion in the sensitivity analysis (Section 2.3). For example, with an instrument capable of 1% optical resolution, the attenuation caused by $C = 10^{-4}$ g/cc has to cause an attenuation of at least 5% in order to achieve 20% accuracy. The transmission equation then becomes

$$\frac{I}{I_o} = 0.95 = \exp\left(\alpha(10^{-4} \text{ g/cc})\right) \tag{7}$$

for which $\alpha = -513$ cc/g (which can be achieved by tailoring the pathlength,

9
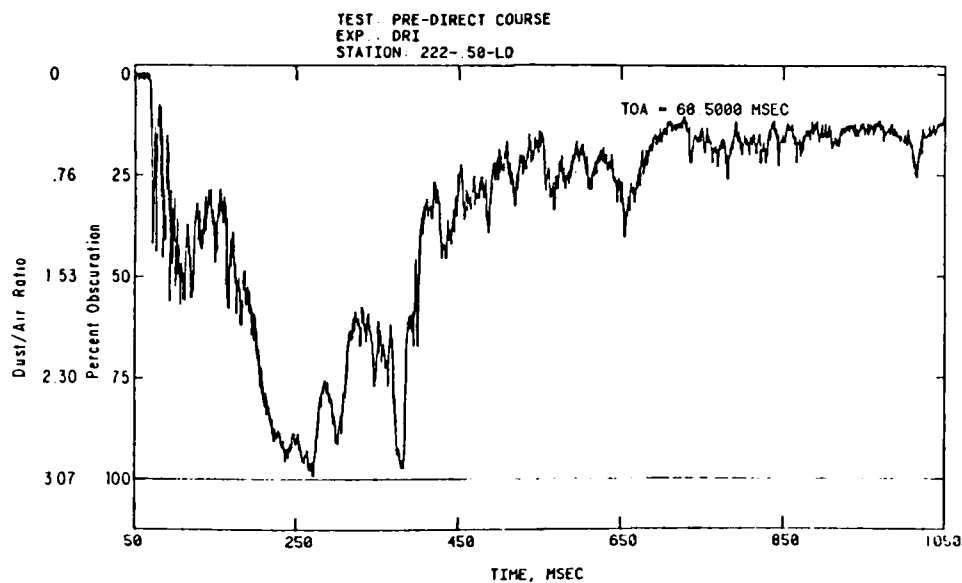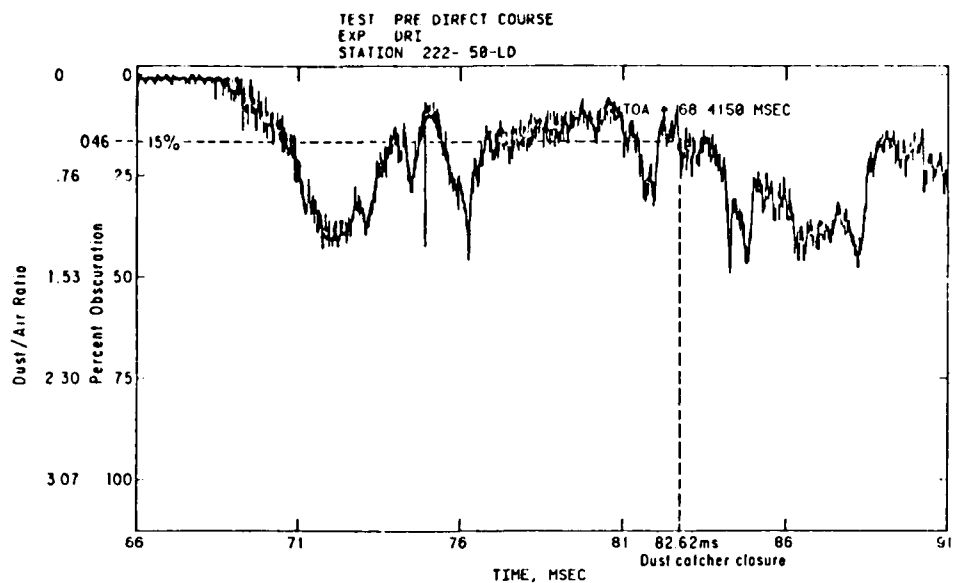
Figure 3.1   Laser-diode Dust Measurements
from the Pre-Direct Course Event

10

given the term $\frac{\bar{Q}}{\rho d_{32}}$). A mass density $C = 10^{-2}$ g/cc would then cause a transmission ratio $I/I_0 = 6 \times 10^{-3}$, which corresponds to a 22 dB optical dynamic range. The necessary frequency response can also be estimated from the Pre-Direct Course data of Figure 3.1, where it is apparent that no sigificant fluctuation in dust density occurred in less than 0.5 ms. Thus, a 2 kHz sampling rate was considered adequate. An additional design goal was to have the capability of measuring and accounting for the effects of non-incident light (e.g., scattered sunlight, the fire ball, or glowing debris) and electronic zero drift. This can be achieved by operating the probe with a pulsed optical signal.

The physical requirement for an aerodynamic measurement station design suggested using a single, small diameter lens to collimate and to focus the beam.

3.2 Initial Component Selection

A literature survey showed that optical extinction measurements of dust density had been successfully achieved using a HeNe laser,[5] a laser diode,[2] and an infrared LED[6,7] light sources, and photodiodes[2,5,6,7] and phototransistors[7] as detectors. There was no inherent performance advantage to any of these systems and none of the systems incorporated fiber optics, so it was not evident which type of source or detector was most suitable. Therefore, at least one of each type of light source and detector was tested in the development of the probe. A variety of optical fibers with different core diameters and core materials were tested, since it was uncertain how these parameters would affect power transmission or coupling efficiency. AMP Optimate fiber optic connectors and device mounts were chosen since they accommodated the broadest variety of fibers, and they were readily available at low cost. The remaining optical support equipment such as lenses, holders and positioners was available in-house. The initial selection of components is shown in Table 3.1.

11

Table 3.1 Components Selected for Testing

DEVICE	DESCRIPTION
Sources	
1. HeNe Laser	0.5 mW λ = 633 nm, 1 mm Collimated Beam
2. Honeywell SPX 4689-002 } Honeywell SPX 4689-003 }	Infrared LED's, λ = 820 nm, Fiber Optic Mount
3. GE F5E1	Infrared LED's λ = 850 nm,
4. NEC NDL30000	Laser Diode, λ = 780 nm P_o = 8.0 mW
5. Mitsubishi ML3131	Laser Diode, λ = 820 nm
Detectors	
1. UDT 125 DP/L	Silicon Photodiode Lensed PV
2. UDT 040A	Silicon Photodiode Lensed PV
3. GE F5D1	Photodarlington Fiber Optic Case PV
4. Honeywell SPX 4691-002	Silicon Photodiode Fiber Optic Case PC
5. Honeywell SPX 4692-002	Silicon Photodiode Fiber Optic Case PC
6. Honeywell SPX 4690-002	Integrated Detector

Optical Fibers	Core Dia.	Attenuation @	NA
1. Newport Research FMLD	100 μ	4.5 @ 850 nm	.3
2. DuPont Crofon OE1040	1000 μ	500 @ 620 nm	.53
3. Nissho Iwai SH4001	1000 μ	300 @ 620 nm	.50
4. General Fiber Optics PS-400-A	400 μ	8 dB @ 820 nm	.3
5. Quartz Products QSF 600A	600 μ	5 dB @ 820 nm	.27

Fiber Optic Connectors and Couplers	
1. AMP 1-530530-1	400 μ Ferrule
2. AMP 530530-5	600 μ Ferrule
3. AMP 227285-7	100 μ Ferrule
4. AMP 530530-2	1000 μ Ferrule

Device Mounts	
1. AMP 530563-1	Mount for TO-18, TO-46, TO-52 Devices
2. AMP 530-565-1	Mount for T1 3/4 Devices
3. AMP 227324-1	Free Hanging Coupling

3.3 General Development Plan

The selection of an effective combination of optical components was achieved through a laboratory evaluation of candidate configurations. The first step in the evaluation of a configuration was to check that sufficient optical power was transmitted through the system and that an adequate degree of collimation of the interrogating beam was achieved. Then the candidate configurations were tested to determine their extinction coefficient and their performance characteristics. Specifically, the transmission ratio I/I_o across a known path length was measured at several independently measured dust mass concentrations. This data was plotted in the form I/I_o = exp (αC), and a least squares fit of the transmission equation (5) was performed.

12

The path length ℓ could be factored out of this curve fit, allowing the probe's measurement range to be predicted as a function of path length. This path length scaling was verified by performing calibrations using different path lengths. In addition, the dust sample's particle distribution and specific gravity were measured by an independent service laboratory, and the terms ℓ, ρ and d_{32} were used to provide an a priori estimate of α for comparison with the measured laboratory values.

3.4 Test Facility and Calibration Procedure

A test facility which provided a controlled density dust flow was designed and fabricated. This facility's design was based upon the dust flow calibration apparatus used by Ausherman.[5] In brief, dust flows down a vertical channel, past the probe and through a tube of known volume. The dust density is measured by simultaneously closing off the top and bottom of this tube, weighing the captured dust and dividing the dust weight by the tube volume.

The test facility (Figure 3.2) consists of an eight foot high vertical flow channel with an 8 inch by 8 inch square cross section. The front face of the flow channel is plexiglass, allowing the dust flow to be observed. A 1,000 in^3 capacity ($\sim$ 50 lbs) hopper at the top of the flow channel holds the dust sample. The dust flow out of the hopper is controlled by a variable orifice made of two perforated plates which slide relative to each other. As the plates slide, the holes on the two plates overlap, allowing dust to flow out in a uniform distribution across the entire flow channel cross section.

Adjustable stops on the plates control the degree of overlap, and thus the flow rate. Dust mass concentrations from $\sim 2 \times 10^{-4}$ to 8×10^{-3} g/cc were achieved in this manner. As the dust falls down the flow channel it is uniformly dispersed by screens at 4 inch intervals. These screens are removable so that different mesh sizes can be used with different soil types. The optical probe protrudes into the flow through slots in the flow channel wall located just below the lowest screen. The optical probe is aligned and held at a preset spacing by magnetic bases on a metal table surface outside the flow channel (Figure 3.3).

13
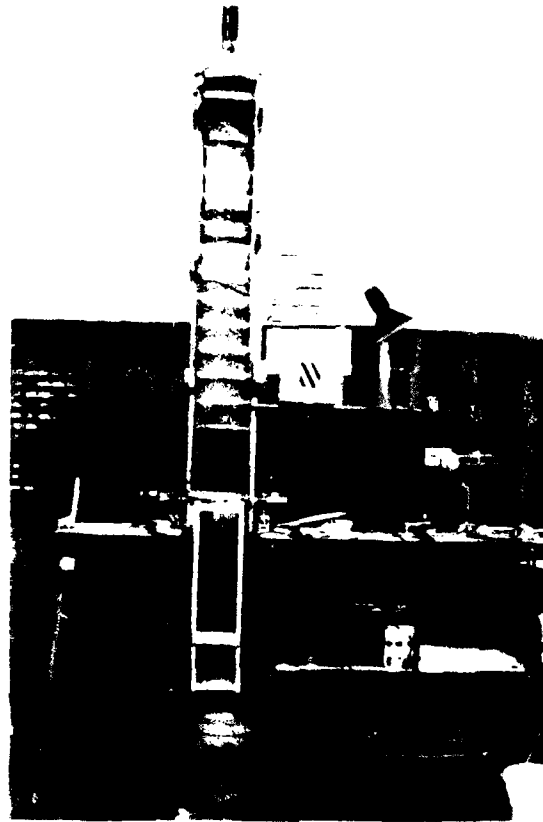
Figure 3.2 Dust Flow Test Facility

The dust is collected in an acrylic tube (5.75 inches in diameter by 23.125 inches tall) held in a vertical orientation concentric with the flow channel walls. Dust flows freely around and through the tube until a dust density measurement is made by simultaneously closing off the top and bottom of the tube with sliding blades. The dust flowing through the tube prior to closure is trapped and falls into a container held on the bottom blade.

The test procedure used to acquire light transmission vs. dust density data was as follows. First the stops on the hopper orifice were set for an appropriate flow rate. Before initiating the dust flow, the detector electronics were zeroed (if necessary), the optical windows were cleaned, and the voltage V_0 at the unattenuated intensity I_0 was recorded.

14
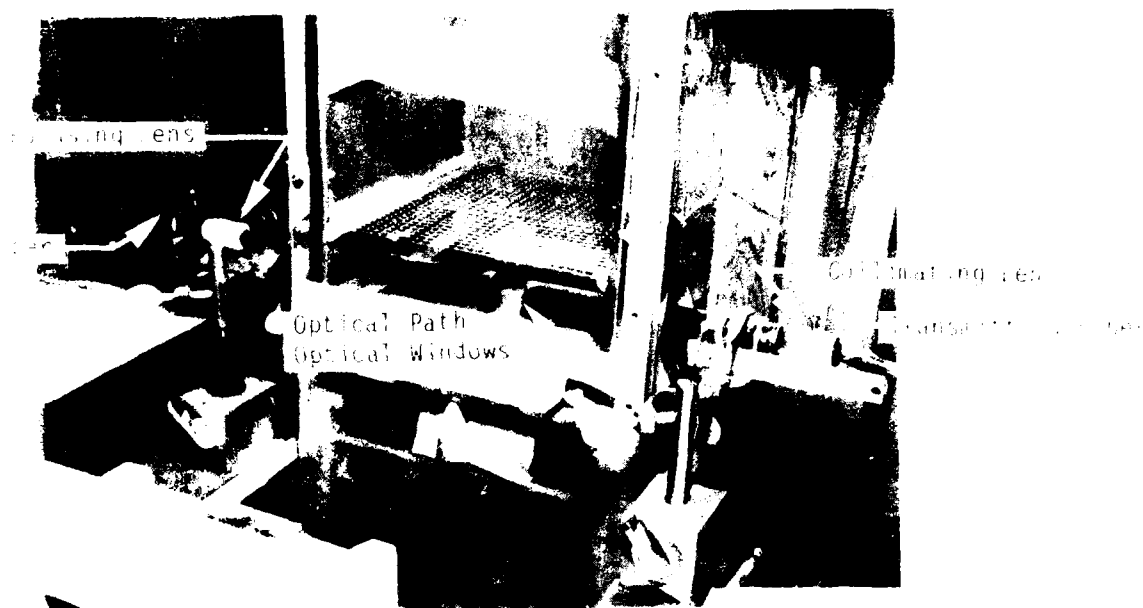
Figure 3.3   Dust Probe Placement in Test Facility

After the hopper orifice opened, dust was allowed to flow freely until the flow appeared well dispersed, and the probe voltage output displayed on a digital multimeter had stabilized. This usually only took a few seconds. The computer controlled data acquisition program then digitally sampled the probe output voltage (typically 600 samples at 300 Hz). When the data acquisition was completed, the dust collection tube was immediately sealed off. The data acquisition time span was set so that a particle falling at slightly less than the terminal velocity of a sphere with the mean dust particle diameter (30 cm/sec) would travel the height of the dust collector tube. This meant that a particle passing the probe at the beginning of the data acquisition would just reach the bottom of the tube at the end of the data acquisition, and the dust trapped in the tube would correspond with the dust that had contributed to the transmission measurement.

15

The post-flow value of V_0 was also recorded to assess dust adhesion to the windows. If there was a significant decrease in V_0 due to dust coating, the post-flow value of V_0 was used. The value of V_0 was entered into the computer, which then plotted the normalized voltage history $V/V_0 = I/I_0$ and computed the average and rms normalized voltages. Typical hard copy outputs are shown in Figure 3.4.
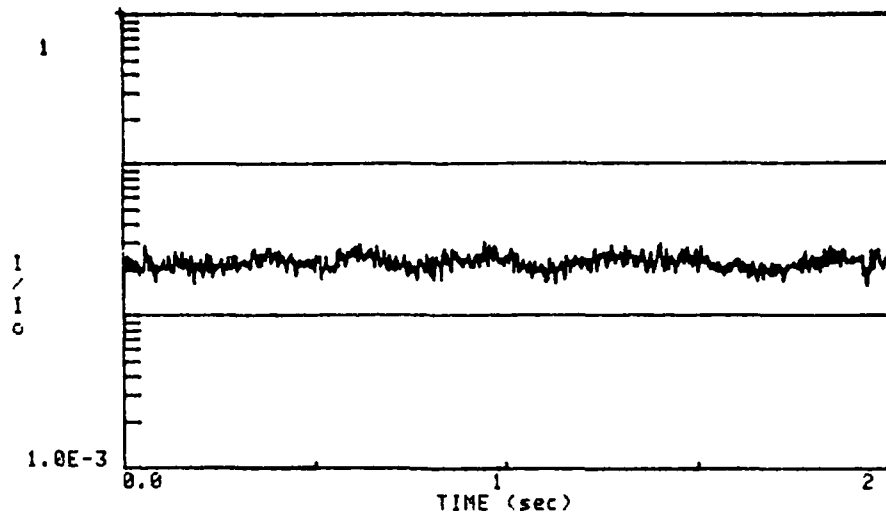
DIODE OUTPUT VS TIME

```
RUN NUMBER  27                 MEAN I/Io =  +2.2441E-002
C1 = +1.0000E+000              RMS I/Io  =  +2.5128E-003
C2 =   0.0000E+000             MEASURED WEIGHT = 70.01
FREQUENCY = 300               CALCULATED DENSITY =  +7.1970E-003
# OF SAMPLES = 601
MEAN VOLTAGE =  +2.2441E-001
```
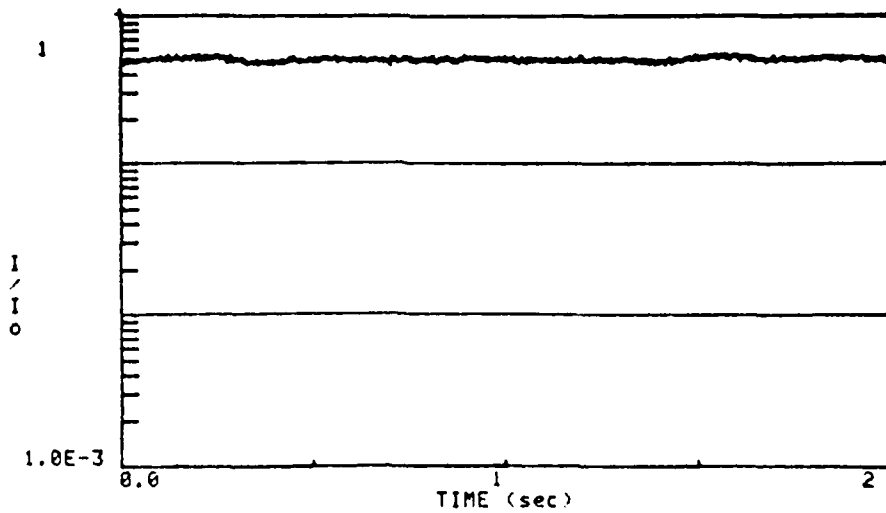

DIODE OUTPUT VS TIME

```
RUN NUMBER   6                 MEAN I/Io =  +5.1681E-001
C1 = +1.0000E+000              RMS I/Io  =  +1.5743E-002
C2 =   0.0000E+000             MEASURED WEIGHT = 10.24
FREQUENCY = 300               CALCULATED DENSITY =  +1.0527E-003
# OF SAMPLES = 601
MEAN VOLTAGE =  +5.1681E+000
```

Figure 3.4 Typical Dust Probe Outputs

17

SECTION 4. EXPERIMENTAL RESULTS AND DISCUSSION

During the experimental development of the optical dust probe, several combinations of optical emitters, optical fibers, collimating optics, and detectors were tested. These tests and the pertinent results are summarized in Table 4.1

The dust density vs. transmission test results obtained with the preliminary probe configurations are shown in Figures 4.1 through 4.3 (the final configuration will be discussed later). It is apparent that each configuration provided data that followed the form of the transmission equation $I/I_0 = e^{-\alpha C \ell}$.

Figure 4.3 shows that the calibration curves of a given probe configuration scale with a change in the optical path length, as expected.

During the development program, the evaluation of the various components provided some clear guidelines for the selection of the final probe configuration. For example, it was found that while both a HeNe laser and an infrared LED provided sufficient optical dynamic range to measure the desired range of dust densities, the LED was clearly superior for the present application since it

    (1)   is less expensive ($\sim$ \$20 vs. $\sim$ \$370),

    (2)   is much more compact,

    (3)   requires less power, e.g., can be powered by batteries

    (4)   is more easily coupled to an optical fiber (the chosen LED is factory mounted in a fiber compatible housing)

    (5)   can be electronically pulsed to allow ambient light noise and electronic zero drift to be measured.

A GaAlAs infrared (820 nm) LED was chosen as the optical emitter (Figure 4.4). It was driven by a simple transistor switching circuit which allowed continuous or pulsed operation (Figure 4.5).

18

Table 4.1 Summary of Test Performed

OPTICAL EMITTER	TRANSMITTING FIBER	COLLIMATING OPTICS	RECEIVING FIBER	DETECTOR	COMMENTS
Laser Diode NED NDL 3000 Mitsubishi ML3101	--	--	--	--	Laser diodes proved delicate, difficult to stabilize.
HeNe Laser Melles Griot LP-05	--	--	--	UDT 125 DP/L Silicon Photodiode External Voltage Amplifiers	Verified facility performance.
HeNe Laser Melles Griot LP-05	Direct Coupled CROFON OE 1040	Collimating - Compound System (1) 17.6 mm dia. 15.9 mm f.l. (1) 50 mm dia. 175 mm f.l. Focusing lens (1) 50 mm dia. 30 mm f.l.	--	UDT 125 DP/L Silicon Photodiode External Voltage Amplifiers	Demonstrated use of transmitting fiber. Showed difficulty of collimating light from large core fibers
HeNe Laser Melles Griot LP-05	Direct Coupled CROFON OE1040	Collimating - Compound System (1) 17.6 mm dia. 15.9 mm f.l. (1) 50 mm dia. 175 mm f.l. Focusing lens (1) 50 mm dia. 30 mm f.l.	CROFON OE 1040	UDT 125 DP/L Silicon Photodiode External Voltage Amplifiers	Demonstrated use of receiving fiber.
HeNe Laser Melles Griot LP-05	Direct Coupled CROFON OE 1040	Collimating - Compound System (1) 17.6 mm dia. 15.9 mm f.l. (1) 50 mm dia. 175 mm f.l. Focusing lens (1) 50 mm dia. 30 mm f.l.	CROFON OE 1040	UDT 125 DP/L Silicon Photodiode External Voltage Amplifiers	Showed path length scaling of transmission equation.
IR LED GE F5E1	Pigtailed Quartz Products OSF 600A	--	--	--	Sufficient power launched, based on previous experiments. Extremely time-consuming process to couple fiber to LED.
IR LED Honeywell SPX 4689-003	Ferruled General Fiber Optics PS-400-A	Collimating lens 17.6 mm dia. 15.9 mm f.l. Focusing lens 18 mm dia. 33 mm f.l.	Ferruled Quartz Products QSF-600A	UDT 125 DP/L Silicon Photodiode In Transimpedance Circuit	Final configuration.
IR LED Honeywell SPX 4689-003 Pulsed Operation	Ferruled General Fiber Optics PS-400-A	Collimating lens 17.6 mm dia. 15.9 mm f.l. Focusing lens 18 mm dia. 33 mm f.l.	Ferruled Quartz Products QSF-600A	UDT 125 DP/L Silicon Photodiode In Transimpedance Circuit	Demonstrated pulsed operation. Illustrated optical dynamic range and system frequency response.
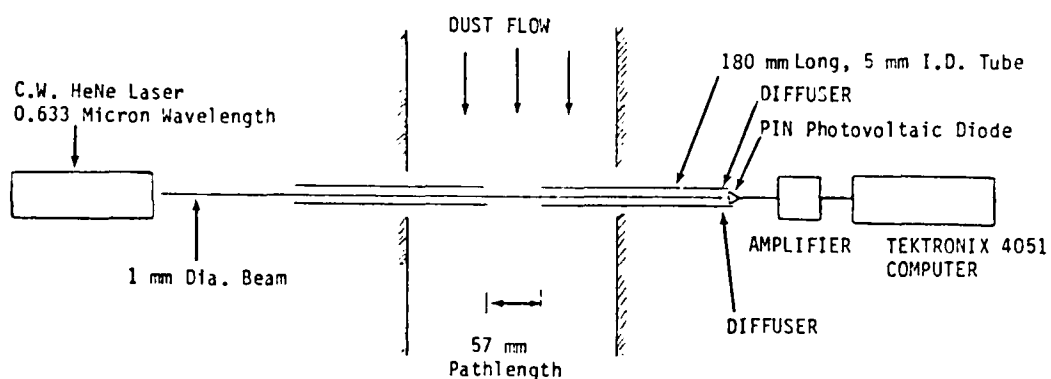
Present Experimental Arrangement
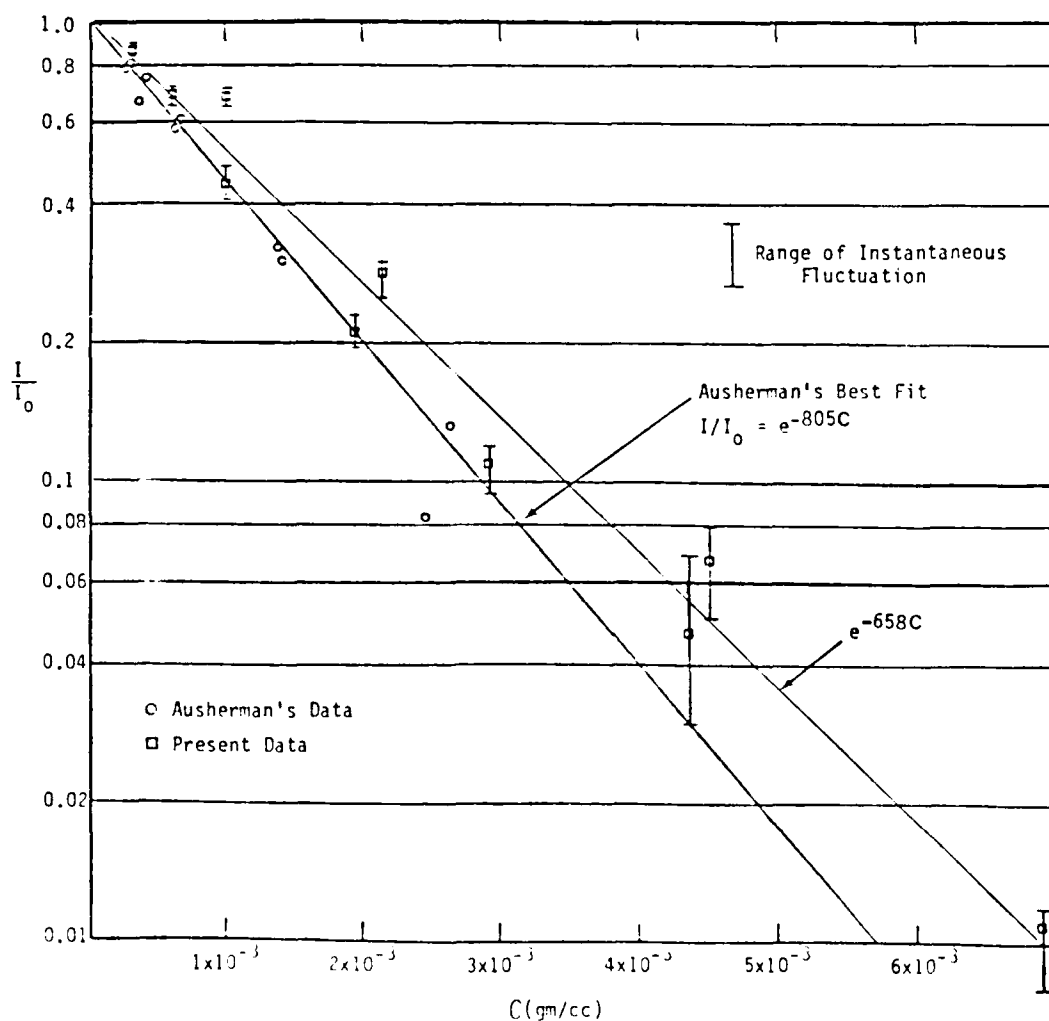
Figure 4.1 Repeat of Ausherman Calibration

C.W. HeNe Laser
0.633 Micro Wavelength

DUST FLOW

15 mm Dia. Collimated Beam

180 mm Long, 16 mm I.D. Tube

PIN Photovoltaic Diode

1 mm Dia. Beam

1 Meter length
1000 μm Core
Plastic
Optical
Fiber

Collimating
Lens

57 mm
Pathlength

DIFFUSER

FOCUSING LENS

AMPLIFIER

TEKTRONIX 4051
COMPUTER

I/I_0

"Eyeball" Best Fit
$I/I_0 = e^{-920C}$

C (gm/cc)
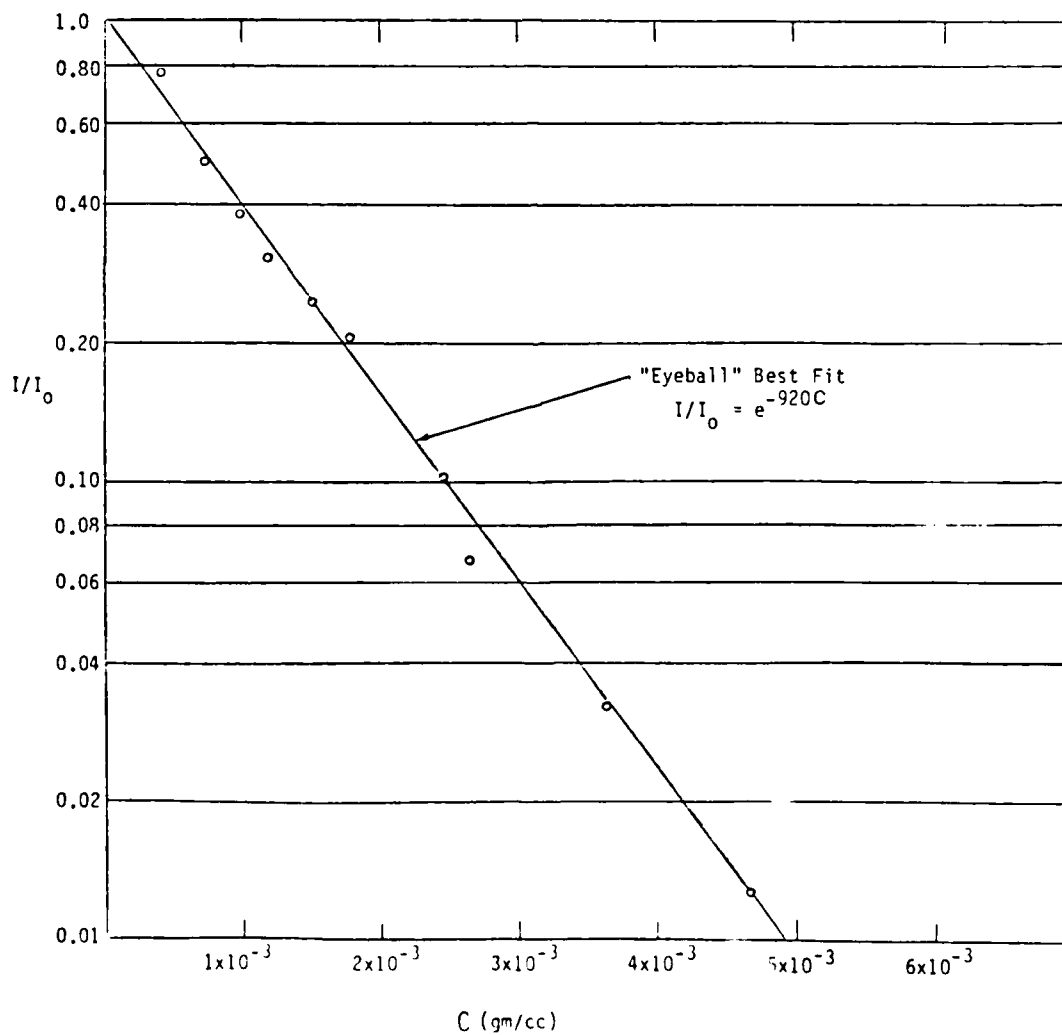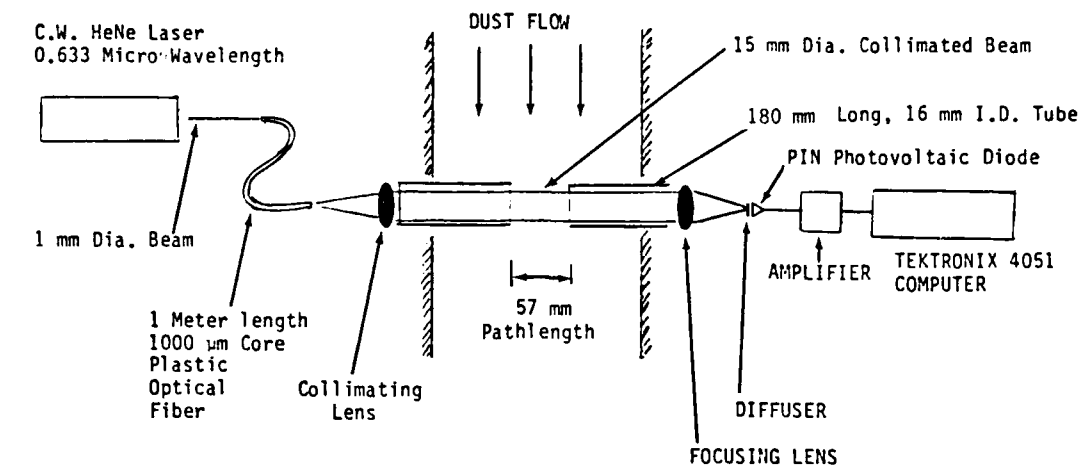
Figure 4.2   Experimental Arrangement Using Transmitting Fiber

DUSTY FLOW

11mm Aperture

Optical Windows

Inner Surfaces Painted Black

PIN Photovoltaic Diode

Amplifier

0.5mW CW HeNe Laser

Collimating Lens

Path Lengths
57mm
26mm

Focusing Lens

Tektronix 4051 Computer

1 Meter Crofon OE 1040 Fiber

2 Meters Crofon OE 1040 Fiber

FIT OF DATA OBTAINED WITH PATH LENGTH = 2.6 cm

CURVE PREDICTED BY SCALING DATA OBTAINED WITH PATH LENGTH = 5.7 cm

FIT OF DATA OBTAINED WITH PATH LENGTH = 5.7 cm

$\frac{I}{I_0}$

$C(g/cc) \times 10^{-3})$

LEAST SQUARES CURVE FIT

OTTAWA 12-13/15 **LONG PATH LENGTH**

NUMBER OF POINTS=   7
----
1) FOR Y ON X, LN(I/IO)=ALPA*CM   , ALPHA =   -447 1191
2) FOR Y ON Y, CM=(1/ALPHA)*LN(I/IO) , ALPHA =   -447 2056
3) FOR I=A*EXP(B*X) , A =   1.042577   B =   -454 6432

OTTAWA COMPOSITE **SHORT PATH LENGTH** 12/13

NUMBER OF POINTS=   30
----
1) FOR Y ON X, LN(I/IO)=ALPA*CM   , ALPHA =   -1053 695
2) FOR X ON Y, CM=(1/ALPHA)*LN(I/IO) , ALPHA =   -1065 820
3) FOR I=A*EXP(B*X) , A =   1 098048   B =   -1088 778

Figure 4.3 Experimental Demonstration of Path Length Scaling
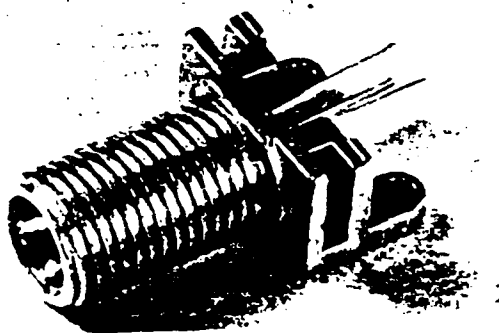
Figure 4.4 Infrared LED Light Source
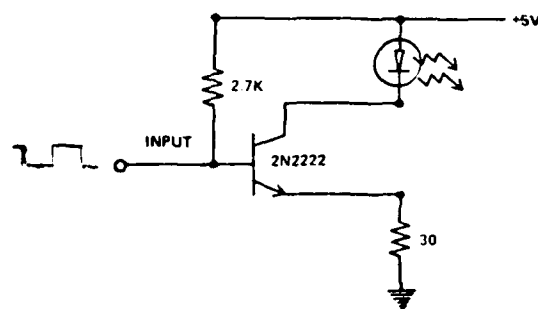
Figure 4.5 LED Driver Circuitry

Experiments with coupling different fibers to the LED showed that there was a trade-off between the power launched through an optical fiber of a given core diameter and the degree of collimation attainable with the fiber. This is because the larger the fiber diameter, the less it acts as a point source. A 400 μm diameter transmitting fiber provided a good compromise. A 600 μm core was used for the receiving fiber since the larger fiber face reduced vibration sensitivity and increased coupling efficiency. Both optical fibers were terminated with AMP Optimate ferrules, allowing them to be easily and repeatably coupled (Figure 4.6).
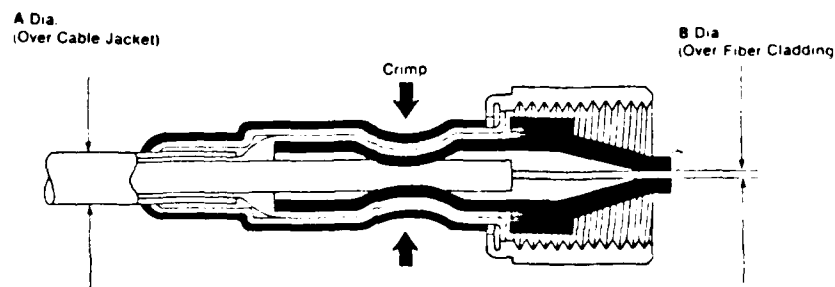
Figure 4.6 Fiber Termination and Connector

A silicon photodiode operating in the photovoltaic mode in a transimpedance circuit was chosen as the optical detector. The output voltage of this circuit is linearly proportional to intensity (Appendix C) which allows direct determination of the transmission ratio from measured output voltage ratio. The p todiode was mounted in an AMP active device mount (Figure 4.7) and wired directly into a transimpedance amplifier circuit (Figure 4.8) to reduce electronic noise and increase the frequency response.

These components were combined to form the final optical probe configuration as schematically illustrated in Figure 4.9.
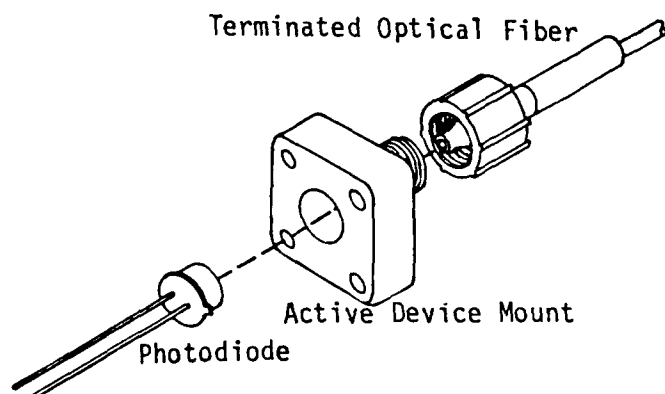
Figure 4.7 Optical Detector Mount
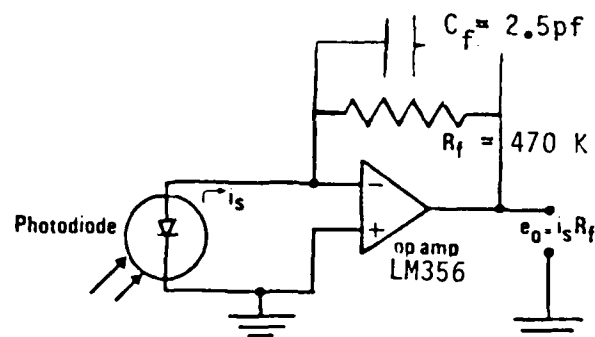
Figure 4.8 Transimpedance Amplifier Circuit
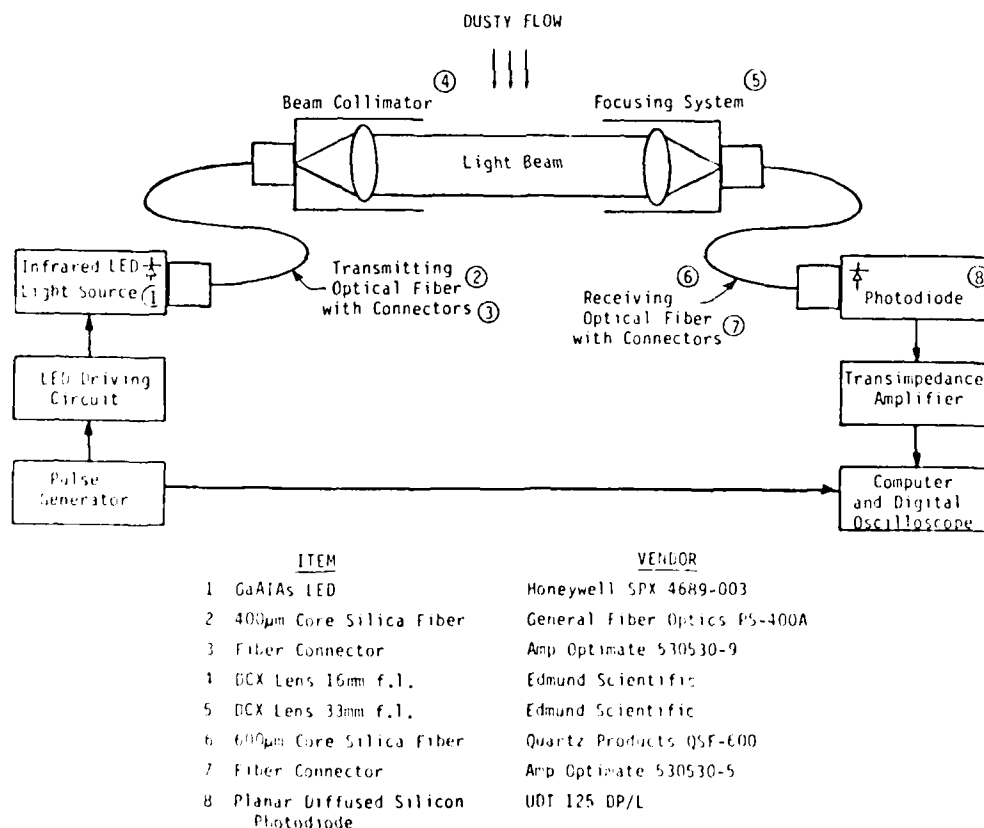
Figure 4.9 Schematic of Final Probe Configuration

ITEM		VENDOR
1	GaAlAs LED	Honeywell SPX 4689-003
2	400μm Core Silica Fiber	General Fiber Optics PS-400A
3	Fiber Connector	Amp Optimate 530530-9
4	DCX Lens 16mm f.1.	Edmund Scientific
5	DCX Lens 33mm f.1.	Edmund Scientific
6	600μm Core Silica Fiber	Quartz Products QSF-600
7	Fiber Connector	Amp Optimate 530530-5
8	Planar Diffused Silicon Photodiode	UDT 125 DP/L

24

The final fiber optic dust probe configuration was calibrated using graded Ottawa Sand and a soil sample from the Pre-Direct Course test bed (Figure 4.10). In each case, the measured transmission ratio vs measured dust mass concentration data was fit (in a least squares sense) th a curves of the form

$$C = \ln (I/I_0)/\alpha\ell .$$ (8)

For the calibrations with Ottawa Sand, the best fit is

$$C = \ln (I/I_0)/-209.5 \ \ell .$$ (9)

The relative deviations about the best fit curve curve were calculated, and it was found that 90% of the points fell within ± 30% of the curve fit.

Similarly, the best fit of the calibrations using the Pre-Direct Course soil sample are

$$C = \ln (I/I_0)/-93.5 \ \ell$$ (10)

In this case, 90% of the data fell within ±25% of the cuve.

Thus, based on these calibrations, the natural logarithms of the transmission ratio as a predictor of dust mass concentration provides a accuracy of approximately ±30%.

Extinction curves for the Pre Direct Course soil sample and the Ottawa sand were also calculated from the average of the pre-test and post-test particle size distribution and particle specific gravity data returned by the independent testing laboratory (Appendix A). Putting these results in the form of the extinction equation and assuming $\bar{Q} = 2$, the transmission equation for Ottawa sand yields

$$C = \ln (I/I_0)/-119.9 \ \ell$$ (11)

25

Figure 4.10   Calibration of Final Probe Configuration Using Ottawa F-140 Sand and a Soil Sample From the Pre-Direct Course Test Bed

26

and the transmission equation for the Pre-Direct Course soil sample yields

$$C = \ln (I/I_o)/-57.6 \, \ell \tag{12}$$

The transmission data for the two dust types varies with the term $\frac{1}{d_{32}\rho}$ as expected. This is evident in the fact that the ratio of the extinction coefficient terms for the two dust samples as determined by the soil analysis of the term $\frac{1}{d_{32}\rho}$ is

$$\frac{\text{Ottawa}}{\text{Direct Course}} = \frac{119.4}{57.6} = 2.1 \tag{13}$$

and the calibrations yield the extinction coefficient ratio

$$\frac{\text{Ottawa}}{\text{Direct Course}} = \frac{208.7}{92.5} = 2.3 \tag{14}$$

However, it is evident that the extinction coefficients calculated from soil analysis differed markedly from the extinction coefficients determined by calibration, as shown in Figure 4.11. For the Ottawa sand, the dust mass concentration at a given transmission as calculated from the soil analysis is 75% higher than the dust mass concentration determined by the calibration curve. For the Direct Course dust sample, the dust mass concentration calculated from the soil analysis is 62% higher than the dust mass concentration determined by the calibration curve.

These differences are not explained by the variation of $\bar{Q}$ between 1 and 2 since varying the value of $\bar{Q}$ from the assumed value of 2 to 1 moves the calculated values of the extinction coefficient further away from the measured values. Nor can they be satisfactorily explained by the uncertainties in the two different techniques, as discussed in Appendix B. The exact cause of these differences is not presently known, however it is interesting to note that Cashdollar et al.[7] found that their dust probe calibrations of transmission vs. dust density using a similar dust probe also fell below the curve predicted by particle size and density information (Figure 4.12). Based on the results of the present program it is clear that to maximize the accuracy of the present probe it must be characterized by calibration with a representative dust sample.

27
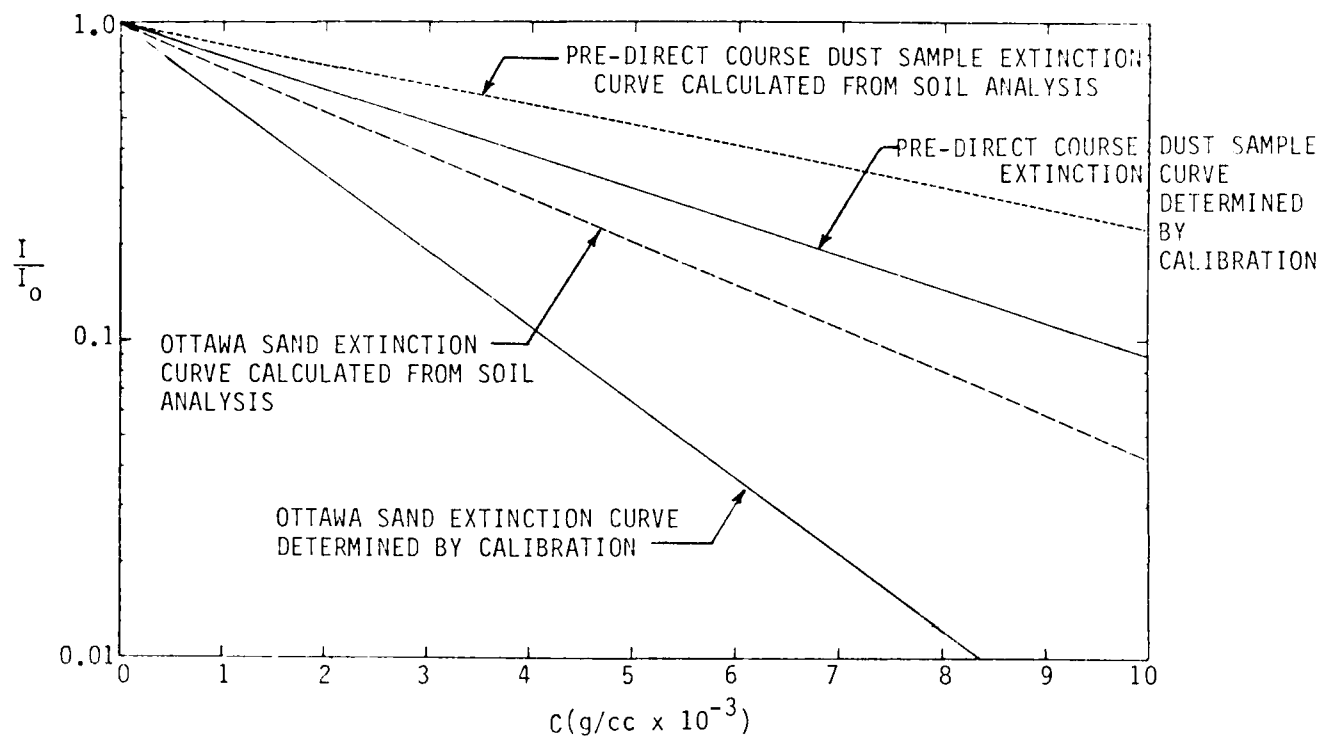
Figure 4.11 Comparison of Extinction Curves Determined by Calibration
and Extinction Curves Calculated From Soil Analysis
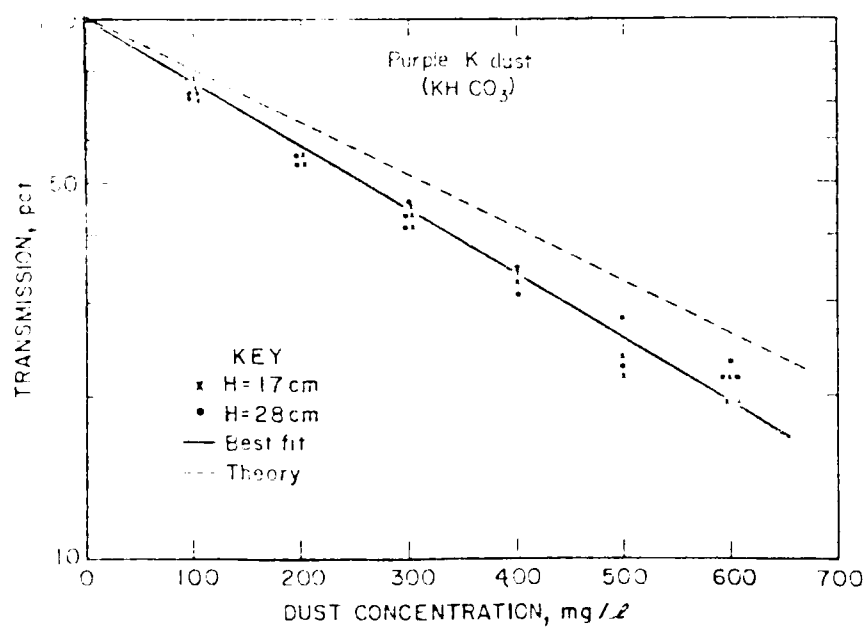
Figure 4.12 Cashdollar's Dust Probe Calibration

28

The pulsed operation of the probe is illustrated in Figure 4.13, which shows a 1 kHz pulsed optical signal transmitted through a dust flow of approximately $\rho_{dust}/\rho_{air} = 3$. The intensity ratio indicated when the LED is turned off represents the total system noise level, including ambient light and electronic noise. The measurement resolution is evident in the bit flip noise when the LED is off. This figure shows the probes 30 dB dynamic range, and the rise and fall times of the system (approximately 10 μ sec).

DIODE OUTPUT vs. TIME

DUST @ ONLY 1KHZ
SAMPLING FREQUENCY = 50000
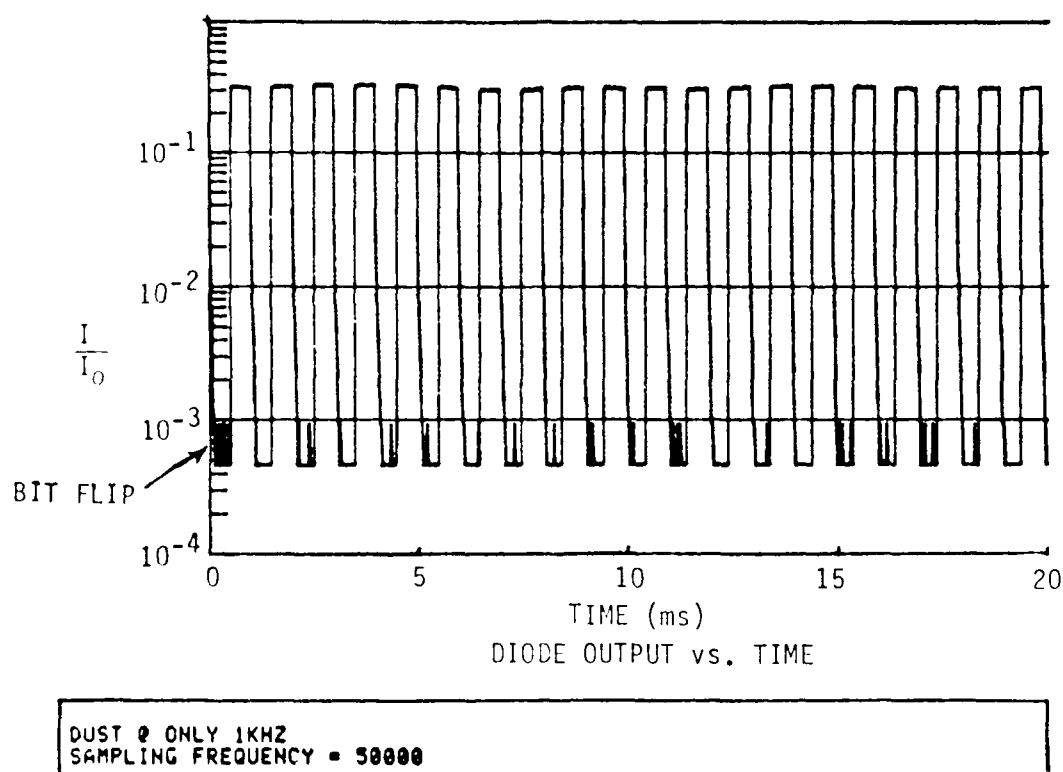
Figure 4.13   Typical Pulsed Operation Dust Probe Output

29

SECTION 5. MEASUREMENT STATION DESIGN

A prototype measurement station to house the optical dust probes during both high explosive field tests and shock tube tests was designed. There were two major requirements that guided this design. First, the measurement station must be able to withstand shock and dynamic pressure loads without allowing a degradation of probe performance. Second, the measurement station design should minimize aerodynamic disturbance of the flowfield at the measurement points. As an aide to meeting these requirements, the design was based on the measurement stations successfully fielded by Carpenter, Hove and Batt in the Middle Gust III and IV boundary-layer velocity profile tests.[8]

Briefly, the measurement station consists of two steel blades which protrude vertically into the flowfield and contain six optical dust probes at various heights. One blade contains the transmitting optics (a single lens collimator) for all six probes and the other blade contains the receiving optics (a single lens collector) for all six probes. The blades are bolted to a steel base plate at a separation which provides the appropriate optical path length for the expected dust densities. In shock tube tests, the optical path length can be modified as the tests progress to optimize the probe's measurement range. A hollow steel sting extends horizontally forward from each blade into the dusty flow at each measurement height. The collimated light beam travels through the sting to a mirrored steel insert which reflects the beam through sapphire windows, across the dusty flow to the other identical sting.

In shock tube applications, the two vertical blades and base plate would be mounted on the shock tube floor. In field applications, the blades and base plate would be bolted to a buried concrete pad. This concrete pad would contain the optical emitters and detectors, and a data acquisition system.

30

5.1 Dust Probe Rake

The dust probe rake blades are 15 inch tall by 12 inch long by 2 inch thick steel plates with a 60° knife edge on the front face (Figure 5.1). Six 1 inch diameter holes are drilled in the front face to hold the lens fixtures and probe stings, as shown in Figure 5.2. The base plate and blades are presently designed to provide optical path lengths of 2.5 cm and 5 cm (Figure 5.3).

SIDE VIEW   TOP VIEW
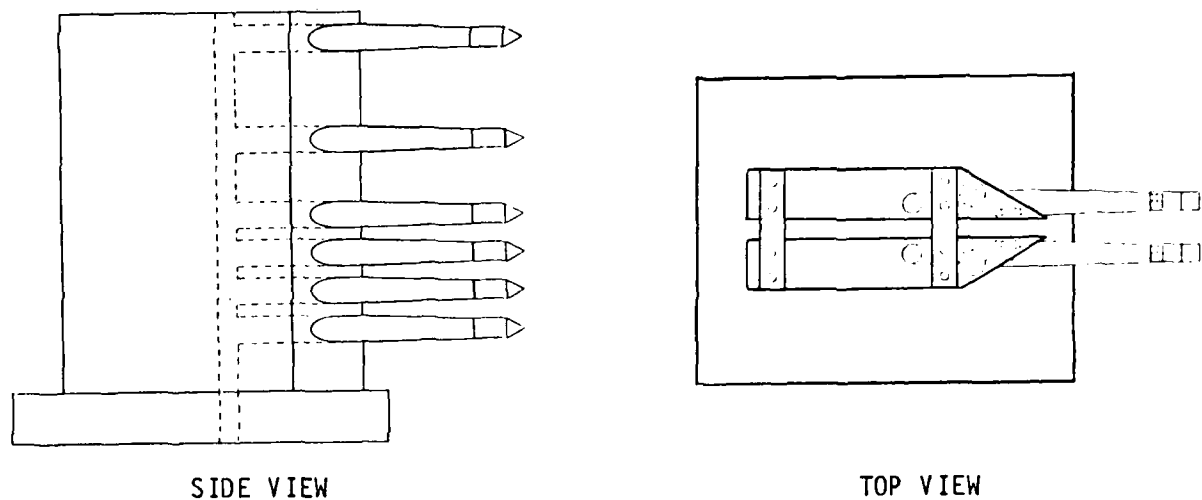
Figure 5.1 Dust Probe Rake Blades
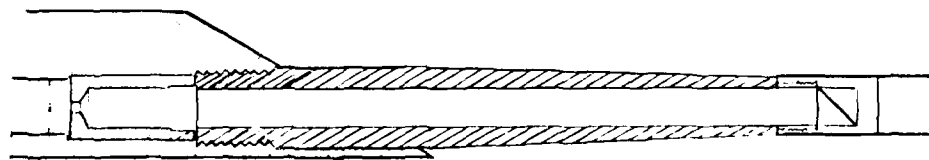
Figure 5.2 Sting and Optical Fixture Mounted in Rake Blade

The sizing of the probe stings was influenced by the diameter of the collimated beam, aerodynamic interference considerations, and structural requirements. The sting's outer diameter determined the minimum probe separation (both vertically and horizontally) due to the aerodynamic restriction that the minimum probe separation be at least 2 probe diameters. The sting's length

31

was, in turn, influenced by the diameter through the aerodynamic rule-of-thumb that the probe support structure should be about 10 probe diameters from the probe tip. Since the expected optical path length (horizontal separation) is ~ 2 inches, the maximum sting diameter is 1 inch. The 10 mm beam diameter used in the final optical probe configuration determined the inner diameter of the probe sting tubes. Based on these considerations and the expected blast loads (as shown in Appendix C) the stings shown in Figure 5.2 were specified. A simple dynamic structural analysis was performed to check the maximum stress and deflections of the stings and blades under ideal and precursor shock conditions.
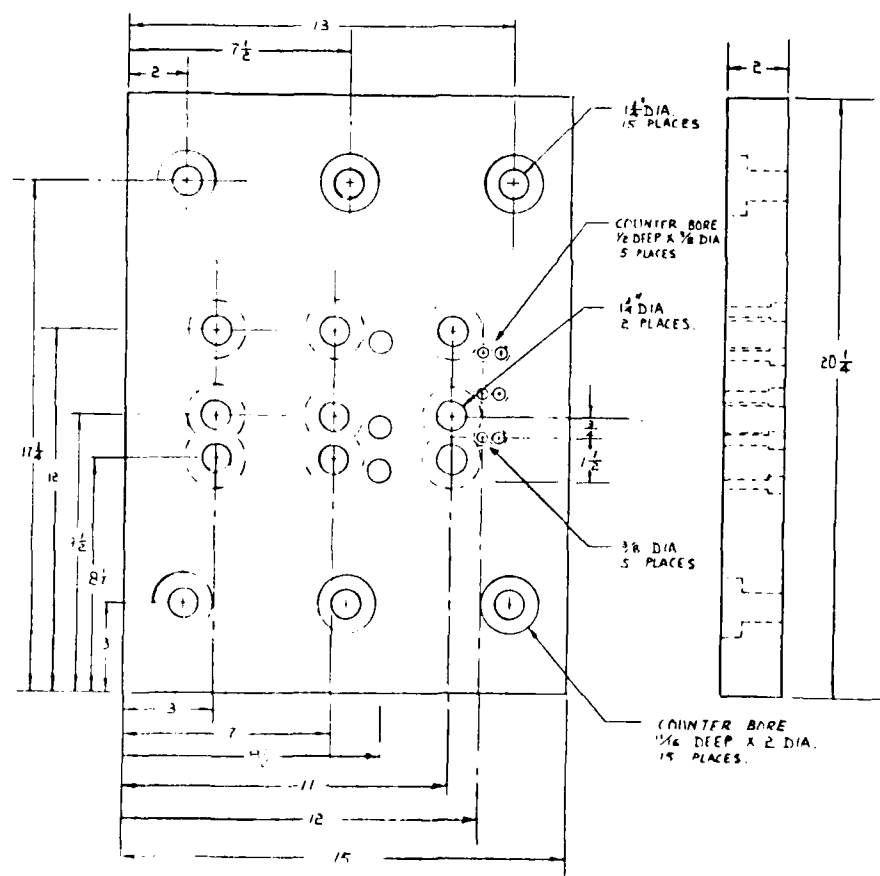
Figure 5.3 Rake Base Plate

5.2 Electronics and Instrumentation Vault

During high explosive field tests the LEDs, LED drivers, photodiodes, trans-impedance amplifiers, and data acquisition system will be shock-mounted in underground steel vaults to protect them from the blast and ground shock. The vault design is similar to that fielded by Carpenter, Hove and Batt[8] in the blast wave boundary-layer measurements for Middle Gust III. The vaults (Figure 5.4) are 36 inch diameter by 36 inch deep steel cylinders with 1/4 inch thick walls and bottom. A 2 inch wide by 1 inch thick flange welded to the top of the cylinder provides an anchor for a 40 inch diameter by 1-1/2 inch thick steel lid. The vaults will be cast into the same concrete block that the probe rake is bolted to, with the vault lid flush with the block surface.
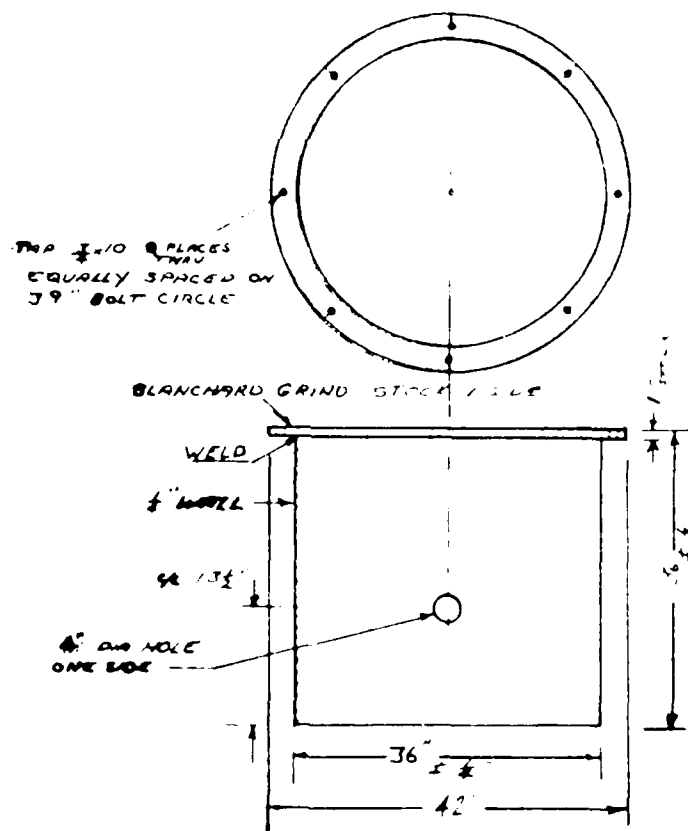
Figure 5.4 Electronic Vaults

33

Rough estimates of the necessary space for the electronics and data acquisition circuitry are: one 8" x 4" board to hold the 6 LEDs with their driving circuitry, one 8" x 4" board to hold the 6 LEDs with their transimpedance amplifiers, and one 12" x 12" board to hold the digital data acquisition and timing circuits. If these components are mounted in a 12" cube there is at least 1 foot of free space around the electronics, which should provide ample room for batteries and shock mounts.

5.3 Digital Data Acquisition System

The data acquisition system for field tests was based on an existing DynaTech portable digital data acquisition system. In the present design, the data acquisition system is a self contained, battery powered unit. The system digitally samples the photodiode voltage and stores the data in dynamic RAM under the control of a microprocessor. After the event, the data is loaded onto a portable digital tape recorder and later reduced on a minicomputer. The components in the expected configuration are shown in Figures 5.5. An Intel 80C31 microprocessor uses software stored in A2716 EPROM to control the system. The data acquisition process is started when an external signal (from the test operator or a separate pressure transducer) provides an interrupt. Then an Analogic MP6112-DR ADC samples the 6 dust probe signals at 5 kHz with 8 bit (1/2 %) resolution. The LEDs are also under the microprocessor control so that the chopped light signal is synchronized with the conversion timing. The data is stored in 64 K dynamic RAM chips. Each chip holds approximately 2 seconds of data from the six probes.

Since it is desirable to have I_0 information from both before and after the event to determine if the optical windows become coated with dust, time requirements dictate the use of at least two 64 K RAM chips.

34
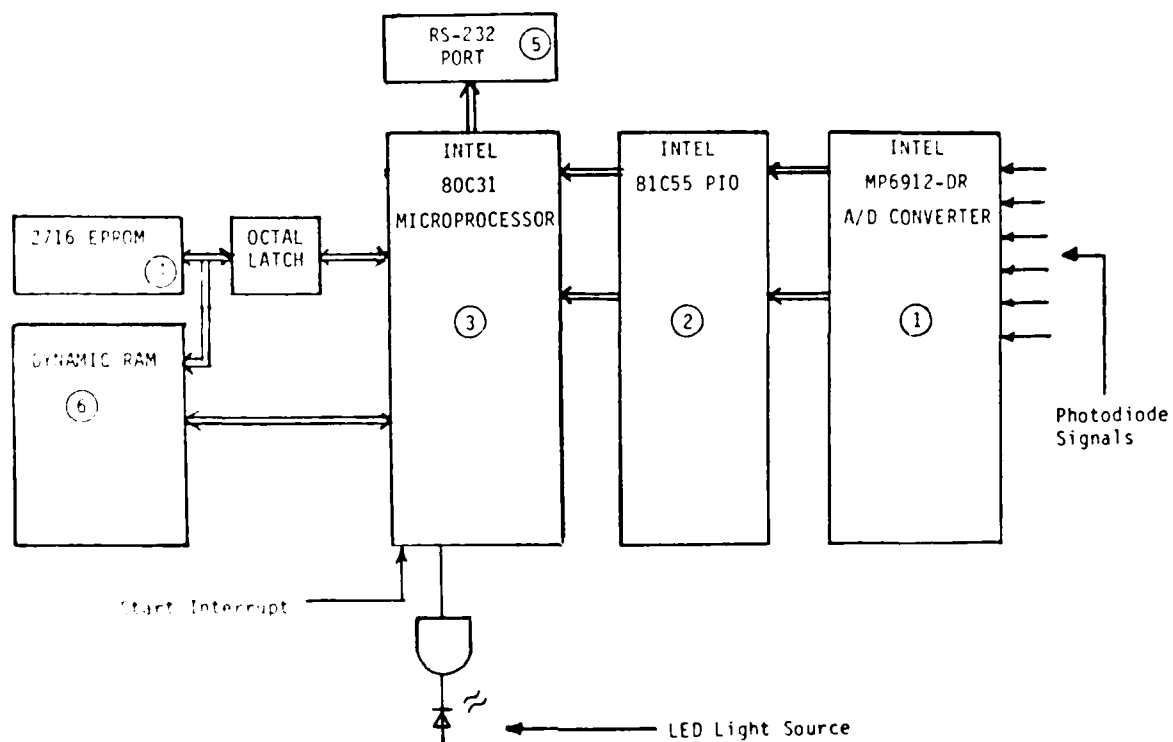
Figure 5.5 Digital Data Acquisition System

35

SECTION 6.   CONCLUSIONS AND RECOMMENDATIONS

Dynamics Technology has completed the phase one development of a fiber optic light extinction probe for measuring the mass concentration of dust lofted in high explosive field tests and shock tube experiments.   It was found that low cost optical components combined with fiber optics provided the necessary optical dynamic range for measuring mass concentrations in the range of 10^{-4} to 10^{-2} gm/cm^3 ($\rho_{dust}/\rho_{air} \sim 0.1$ to 10).   Calibrations using representative dust samples demonstrated that the probe could make repeatable dust mass concentration measurements in this range.   In these calibrations, 90% of the mass concentration measurements fell within 30% of the calibration curves. Laboratory tests demonstrated that the measured range of dust densities could be easily varied by changing the optical path length.   Information from an independent service laboratory determined that the probe's calibration curves scaled to the particle size distributions of the representative dust samples as expected.   However, estimates of dust mass concentration based on the particle size distribution information differed from estimates based on the calibrations by up to 75%.   Therefore, based on the findings of this program, it is recommended that the optical probe be characterized by direct calibration rather than by particle size distribution information.

The optical dust probe in its present configuration is ready for use in dust lofting experiments.   A minor hardware substitution could improve the probe's performance at little additional cost.   This would simply consist of using a Honeywell SPX 4689-004 LED instead of a Honeywell SPX 4689-003 LED.   (The SPX 4689-004 was not used for the experimental prototype was that it was not available in time).   This LED emits about 60% more optical power, and though the present probe demonstrated ample dynamic range, an increase in dynamic range is always desirable.

36

A prototype measurement station was designed which allows dust mass concentration measurements to be made in ideal and precursed shocks with overpressures up to 100 psi. At each station, measurements are made at six heights above the ground (1/2", 2", 3-1/2", 5", 8" and 12"). The measurement station design allows the optical path length to be changed between tests, thus changing the measurement range. In addition, the design includes an underground vault for housing the opto-electronics during high explosive field tests, and a self contained data acquisition system for such tests.

The combination of the fiber optic dust probe and the measurement station are suitable for the upcoming CERF shock tube tests and the Miners Scale Field tests. It is recommended that two stations be fielded, one at a range corresponding to 30 psi overpressure, the other at a 60 psi overpressure, in both these tests.

37

REFERENCES

1. Hartenbaum, B., *"Review of Dust Flow Diagnostics,"* Presentation at Defense Nuclear Agency, January 13, 1982.

2. Wisotski, J., *"Dust Measurements,"* Pre-Direct Course Volume I - Results Report DNA POR 7116-1, pp. 9-108, May 1983.

3. Wuerker, R.F. and Hiu, D.A., *"Optics Diagnostic Experiments,"* Pre-Direct Course Volume I - Results Report DNA POR 7116-1, pp. 197-772, May 1983.

4. Dobbins, R.A. and Jizmagian, G.S., *"Optical Scattering Cross Sections for Polydispersions of Dielectric Spheres,"* J. Opt. Soc. Am., 56, October 1966.

5. Ausherman, D., *"Initial Dust Lofting: Shock Tube Experiments,"* DNA 3162F, September 1973.

6. Conti, R.S. *et al.*, *"Improved Optical Probe for Monitoring Dust Explosions,"* Review of Scientific Instruments, 53 (3) March 1982.

7. Cashdollar, K.L., Liebman, I. and Conti, R.S., *"Optical Dust Probes,"* BuMines R.I.. 9542, 1981.

8. Carpenter, H.J., Hove, D.T. and Batt, R.G., *"Blast Wave Boundary Layer Measurements,"* AFWL-TR-73-211, March 1974.

9. Brode, H.L. *"A Review of Nuclear Explosion Phenomena Pertinent to Protective Construction,"* RAND R-425-PR, May 1964.

APPENDIX A. SOIL SAMPLE ANALYSIS

Both representative dust samples were analyzed by an independent service laboratory to determine their particle density ρ and their mean surface weighted diameter d_{32}. The Pre-Direct Course sample was analyzed before and after the dust probe tests. The Ottawa Sand was only analyzed after the dust probe tests; prior to the tests the suppliers data sheet was used. The particle density ρ was given by the bulk specific gravity, and the mean surface weighted diameter was determined by

$$d_{32} = \frac{\Sigma(N\chi\Delta)}{\Sigma(N\chi\Delta/d)} \qquad (A.1)$$

The data and calculations follow. A summary of the results is given below

Table A.1 Summary of Soil Analysis Results

	PRE-TEST	POST TEST
Ottawa Sand	d_{32} = 0.0078 cm S.G. = Not given	d_{32} = 0.0112 cm S.G. = 2.67
Pre-Direct Course Soil	d_{32} = 0.0190 cm S.G. = 2.57	d_{32} = 0.0213 cm S.G. = 2.59

Table A-2 Independent Soils Laboratory Results

U.S. STANDARD SIEVE NUMBER	MILLIMETER SIZE	% PASSING OR % FINER			% LARGER THAN LISTED MILLIMETER SIZE BUT SMALLER THAN NEXT LARGER SIZE, BASED ON TOTAL DRY WEIGHT		
		SOIL SAMPLE PRE-TEST	SOIL SAMPLE POST-TEST	OTTAWA SAND POST-TEST	SOIL SAMPLE PRE-TEST	SOIL SAMPLE POST-TEST	OTTAWA SAND POST-TEST
4	4.76	100	100	100	0	0	0
8	2.38	100	100	100	0	0	0
16	0.991	98	99	100	2	1	0
30	.589	91	91	100	7	8	0
50	.295	80	80	99	11	11	1
100	.147	59	63	88	21	17	11
200	.074	49	42	31	10	21	57
	.040	41	2.3	0.6	8	29.7	30.4
	.026	37	11	0.6	4	1.3	0
	.015	31	9.9	0.6	6	1.1	0
	.010	27	7.4	0.6	4	2.5	0
	.0079	23	1.5	0.6	4	5.9	0
	.0036	7	1.1	0.6	16	0.4	0
	.0015	6	0.5	0.6	1	0.6	0
	PAN				6	0.5	0.6
	SPECIFIC GRAVITY	2.57	2.59	2.67			

Table A-3. Mean Surface Weighted Particle Diameter Calculations.

Pre-Direct Course Sample, Pre-test

	INTERVAL mm	Δ mm	d mm	χ	$\chi \Delta$	$\chi \Delta/d$
1	2.38 - .991	1.381	1.6855	2	2.762	1.6387
2	.991 - .589	.402	.79	7	2.814	3.562
3	.589 - .295	.294	0.442	11	3.234	7.317
4	.295 - .147	.148	.221	21	3.108	14.06
5	.147 - .074	.073	.1105	10	0.73	6.606
6	.074 - .040	.034	.057	8	0.272	4.772
7	.04 - .026	.014	.033	4	.056	1.697
8	.026 - .015	0.11	.0205	6	.066	3.2195
9	.015 - .01	.005	.0125	4	.02	1.6
10	.01 - .0074	.0026	.0087	4	.0104	1.195
11	.0074 - .0036	.0038	.0055	16	.0608	11.054
12	.0036 - .0015	.0021	.0255	1	.0021	.08235
13	.0015 - .0	.0015	.00075	6	.009	12.

$$\Sigma = 13.142 \qquad \Sigma = 68.996$$

S.G. = 2.57

d_{32} 0.0190 cm

Pre-Direct Course Sample, Post-Test

	INTERVAL mm	Δ mm	d mm	χ	$\chi \Delta$	$\chi \Delta/d$
1	2.38 - .991	1.381	1.6855	1.	1.381	.819
2	.991 - .589	.402	.79	8.	3.22	4.071
3	.589 - .295	.294	0.442	11.	3.23	7.317
4	.295 - .147	.148	.221	17.	2.52	11.38
5	.147 - .074	.073	.1105	21.	1.53	13.87
6	.074 - .040	.034	.057	29.7	1.01	17.72
7	.04 - .026	.014	.033	1.3	.0182	0.552
8	.026 - .015	0.11	.0205	1.1	.012	0.590
9	.015 - .01	.005	.0125	2.5	.013	1.000
10	.01 - .0074	.0026	.0087	5.9	.0153	1.76
11	.0074 - .0036	.0038	.0055	0.4	.00152	0.276
12	.0036 - .0015	.0021	.00255	0.6	.00126	0.494
13	.0015 - .0	.0015	.00075	0.5	.00075	1.000

$$\Sigma = 12.95 \qquad \Sigma = 60.85$$

S.G. = 2.59

d_{32} = 0.0213 cm

A-3

Table A-3. Mean Surface Weighted Particle Diameter Calculations (continued)

Ottawa Sand, Pre-Test

	INTERVAL mm	Δ mm	d mm	χ	$\chi \Delta$	$\chi \Delta/d$
1.	.420 - .297	.123	.3585	0.4	.003	.0084
2.	.297 - .210	.087	.2535	2.0	.174	.6864
3.	.210 - .149	.061	.1795	8.0	.488	2.719
4.	.149 - .105	.044	.1270	35.5	1.562	12.299
5.	.105 - .074	.031	.0895	31.0	.961	10.737
6.	.074 - .053	.021	.0635	12.4	.2604	4.100
7.	.053 - .00	.053	.0265	10.5	.5565	21.000

$$\Sigma = 4.005 \qquad \Sigma = 51.55$$

S.G. = Not Given $d_{32} = 0.0078$ cm

Ottawa Sand, Post-Test

	INTERVAL mm	Δ mm	d mm	χ	$\chi \Delta$	$\chi \Delta/d$
1.	.589 - .295	.294	.442	1.	.294	0.665
2.	.295 - .147	.148	.221	11.	1.628	7.37
3.	.147 - .974	.073	.1105	57.	4.161	37.66
4.	.074 - .040	.034	.057	30.4	1.0336	18.36
5.	.040 -0.26	.014	.033			

$$\Sigma = 7.12 \qquad \Sigma = 63.83$$

S.G. = 2.67 $d_{32} = 0.0112$ cm

APPENDIX B. UNCERTAINTY ANALYSIS

Uncertainties in Extinction Curves Obtained Through Direct Calibration

The measured quantities in the direct calibration of the optical probe are:

(1) the transmission ratio I/I_0 measured as V/V_0 by a photodiode

(2) the mass concentration C as measured by the dust collection tube

(3) the path length ℓ is measured with calipers.

The measurement of I/I_0 is made with a photodiode in a transimpedance circuit so the output voltage is linearly related to the received intensity and $I/I_0 = V/V_0$. It is important, then, to determine whether the relationship between I and V is linear to within a certain percentage over the measurement range of interest. This can be done by examining the electrical equivalent circuit for a PV photodiode (Figure B.1). The flow of photocurrent develops a load voltage which will forward bias the ideal diode, which limits the PV photodiode *response linearity.*
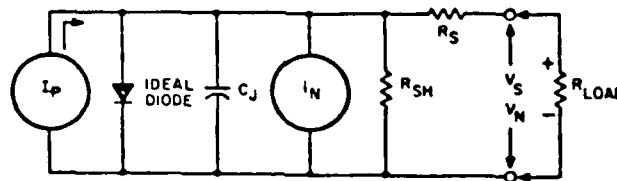
SYMBOLS

I_P = PHOTOCURRENT
C_J = JUNCTION CAPACITY
I_N = EQUIVALENT NOISE CURRENT
R_{SH} = SHUNT RESISTANCE
V_S = SIGNAL VOLTAGE
V_N = NOISE VOLTAGE
R_S = SERIES RESISTANCE

Figure B.1 Photovoltaic Photodiode - Electrical Model

For a given degree of linearity, the maximum photocurrent is given by

$$I_{pm} = 1 \times 10^{-3} \left[\frac{25 \times 10^{-3}}{R_S + R_L}\right] \ln \left[\frac{P \times R_{SH}}{R_S + R_L}\right] \quad A \qquad (B.1)$$

where:

I_{pm} = Maximum photocurrent for P linearity, A

P = Percent linearity desired ÷ 100%
(e.g., for 1% linearity, P = 0.01)

R_S = Series Resistance, Ω

R_L = Load Resistance, Ω

R_{SH} = Shunt Resistance, Ω

The use of an operational amplifier as a "current-to-voltage" converter, (Figure B.2) creates a unique solution to the linearity limitations imposed on PV photodiodes by the terminating load impedance. In this transimpedance configuration, the PV photodiode views a load impedance, equal to the feedback impedance divided by the open-loop amplifier gain,
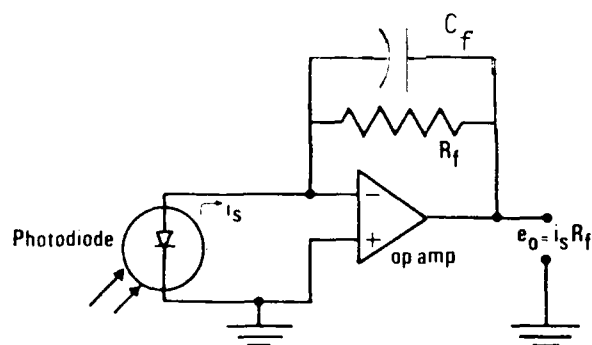

Figure B.2   Photodiode Transimpedance Circuit

$$Z_a = \frac{R_f}{A\left[1 + \left(\omega R_f C_f\right)^2\right]^{1/2}} \qquad (B.2)$$

A very good approximation of photodiode/operational amplifier response linearity can be determined by the substitution of (Z_a) for R_L in Equation (B.1).

Since the voltage output of the transimpedance amplifier is $V_o = I_p R_f$, equation (1) can be rewritten to give the maximum voltage output within a given degree of linearity as

$$V_{o_{max}} = I_{pm} R_f = R_f \left[\frac{25 \times 10^{-3}}{R_S + Z(a)}\right] \ell n \left[\frac{P \times R_{SH}}{R_S + Z(a)}\right] \qquad (B.3)$$

for typical component values,

$$A = 10^5 \qquad (B.4)$$

$$R_S = 1 \ \Omega \ \text{(lead resistance)} \qquad (B.5)$$

$$R_{SH} = 40 \ M\Omega \qquad (B.6)$$

$$R_f = 500 \ k\Omega \qquad (B.7)$$

$$C_f = 2 \ pf \qquad (B.8)$$

$$\omega = 62,831 \ r/s \ (f = 10 \ kHz) \qquad (B.9)$$

the load impedance $Z(a)$ is

$$Z(a) = \frac{5 \times 10^5 \ \Omega}{10^5\left[1 + \left(6.3 \times 10^4 \times 5 \times 10^5 \times 2 \times 10^{-12}\right)^2\right]^{1/2}} = 5.0 \ \Omega \qquad (B.10)$$

and the maximum voltage output is

$$V_{o_{max}} = 5 \times 10^5 \left[\frac{25 \times 10^{-3}}{1 + 5 \ \Omega}\right] \ell n \left[\frac{0.01 \times 5 \times 10^7 \ \Omega}{1 + 5 \ \Omega}\right] = 36 \ \text{volts} \qquad (B.11)$$

Therefore, the typical photovoltaic photodiode in a transimpedance circuit can easily provide a 0 - 10V output signal that provides a linearity within 1% over the entire range.

The measured V/V_0 reflects I/I_0 to within 1% as verified with ND filters. V/V_0 fluctuated over the course of the data acquisition period (Figure B.1) with the degree of fluctuation increasing with increasing dust density. In general, these fluctuations were on the order of $\pm$ 10%.

DIODE OUTPUT VS TIME

RUN NUMBER 15	MEAN I/Io = +1.1576E-001
C1 = +1.0000E+000	RMS I/Io = +1.0000E-002
C2 = 0.0000E+000	MEASURED WEIGHT = 37.30
FREQUENCY = 300	CALCULATED DENSITY = +3.0426E-003
# OF SAMPLES = 601	
MEAN VOLTAGE = +1.1576E+000	
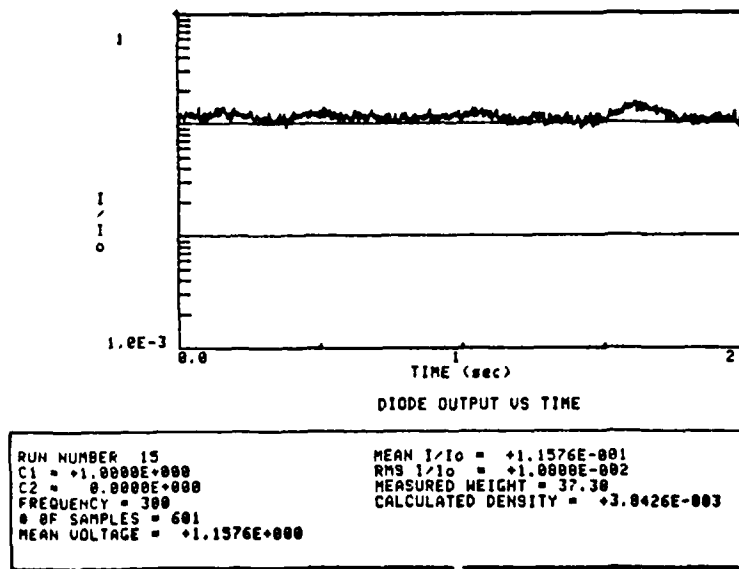
Figure B.3 Typical Fluctuations in Dust Probe Output

Errors in the measured C cannot be determined by repeated measurements made with the same hopper opening, since this does not separate different realizations from variations in the measurement of C. Instead, the uncertainties of the components of the measurement of C were analyzed as follows. The uncertainty in C is given by

$$C = \frac{m}{V} \tag{B.12}$$

$$dC = \left[\left(\frac{\partial C}{\partial m}\, dm\right)^2 + \left(\frac{\partial C}{\partial V}\, dV\right)^2 \right]^{1/2} \tag{B.13}$$

$$dC = \left[\left(\frac{1}{V}\, dm\right)^2 + \left(\frac{m}{V^2}\, dV\right)^2 \right]^{1/2} \tag{B.14}$$

$$\frac{dC}{C} = \left[\left(\frac{dm}{m}\right)^2 + \left(\frac{dV}{V}\right)^2 \right]^{1/2} \tag{B.15}$$

B-4

dV/V is easy to calculate, since the volume of the tube was determined by $V = \pi r^2 h$, where $r = 7.26$ cm $\pm$ 2%, h = 58.7 cm $\pm$ 1%

$$\frac{dV}{V} = \left[\left(\frac{2dr}{r}\right)^2 + \left(\frac{dh}{h}\right)^2 \right]^{1/2} = \left[\left(\frac{2(.02)}{7.26}\right)^2 + \left(\frac{.01}{58.7}\right)^2 \right]^{1/2} \cong 1\% \qquad (B.16)$$

There were three contributors to dm/m. First, there was about 1/8 inch (3 mm) play in blades relative to one another, thus in an extreme case the top blade could lead or lag the bottom blade by 1/8 inch for the aproximate 100 ms closure time, causing a .36 in^2 (2.3 cm^2) area difference to be exposed. For a density C flowing at a velocity V (assumed previously to be 30 cm/s) this Δ area would cause a Δ mass given by $\Delta m = \Delta \dot{m}t = C V \Delta At$, or since C = mass/volume,

$$\Delta m = \frac{mV\Delta At}{Vol} . \qquad (B.17)$$

Therefore, dm/m can be approximated by

$$\frac{dm}{m} = \frac{Vel}{Vol} \Delta At_{closure} = \frac{30 \text{ cm/s} \times 2.3 \text{ cm}^2 \times 0.1 \text{ s}}{9727 \text{ cm}^3} = 7 \times 10^{-4} \qquad (B.18)$$

which is negligible. The second contributor to dm/m is weighing innaccuracies. The weight could be measured to $\pm$ .02 grams. Taking the worst case, a measurement of $C = 1 \times 10^{-4}$ g/cc with the tube volume of 9727 cm^3 means that .97 grams are measured with a $\pm$ 2% error. The third contributor to dm/m is spatial average non-uniformities in the flow during the sampling time. These were not directly measure, but can be assumed to be of the same order of magnitude as the temporal variations observed in the voltage signal, i.e., $\pm$ 10%. Assuming these errors in dm/m are additive, dm/m = 12%. Therefore

$$\frac{dC}{C} = \left((.12)^2 + (.01)^2 \right)^{1/2} \cong 12\% \qquad (B.19)$$

The path length, h, was measured with dial calipers and so can be considered accurate to .01 inch or 1% for the short path length.

Uncertainties in Extinction Curves Calculated From Soil Analysis

The uncertainties in the extinction term $\frac{1}{d_{32}\rho}$ are given by

$$[(\frac{d\ d_{32}}{d_{32}})^2 + (\frac{d\rho}{\rho})^2]^{1/2} \tag{B.20}$$

Since values for d_{32} and ρ were obtained from an independent soils lab and from suppliers data sheets, it is difficult to assess the uncertainties associated with them. One way to estimate the magnitudes is to look at the differences between results obtained at the start of the program and results obtained at the end of the program. The particle specific gravity of the soil sample was given as 2.57 before the test and 2.59 after the test, or a ~ 1% change. (No pretest data on the Ottawa sand specific gravity was available.) An estimate of the uncertainty in particle density is then

$$\frac{d\rho}{\rho} = 1\% \tag{B.21}$$

The value of d_{32} calculated from the suppliers data sheet for Ottawa F-140 (Appendix A) was

$$d_{32} = .0078\ cm \tag{B.22}$$

and the value calculated from the independent laboratory analysis of this Ottawa sand was $d_{32} = 0.0110$ cm. Since the Ottawa sand sent to the laboratory was from a virgin (not used in the calibration) sample of the Ottawa sand, this will be one estimate of the uncertainty in d_{32}

$$\frac{d(d_{32})}{\overline{d}_{32}} = \frac{.011 - .0078\ cm}{.0094\ cm} = 35\% \tag{B.23}$$

The pre-test and post-test results obtained for the Pre Direct Course soil samples were $d_{32} = .0190$ cm and $d_{32} = .0213$ cm respectively. Then a second estimate of the uncertainty in d_{32} is

$$\frac{d\ d_{32}}{\overline{d}_{32}} = \frac{.0213 - .019}{.0202} = 11\%$$ (B.24)

The uncertainty in the term d_{32} can be considered to lie between 11% and 35%, and will be estimated as 20%. The error in the term $\frac{1}{d_{32}\ \rho}$ is the, $(.2^2 + .01^2)^{1/2} \approx 20\%$.

APPENDIX C. MEASUREMENT STATION BLAST LOADS

The blast loading on the measurement station was modeled on the information presented by Brode[9]. Two cases were investigated, a 100 psi overpressure ideal shock and a 100 psi overpressure precursor shock. In the ideal shock case, the pressure jumps to the peak pressure within a fraction of a milli-second. The decay of the pressure pulse is initially dominated by the passage of the shock front itself, then the further decay is dictated by the rate of pressure decrease in the shock wave interior (Figure C.1).
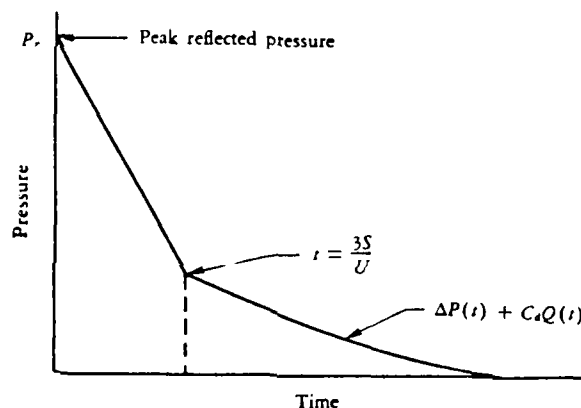

Figure C.1 Fast-Rise or Ideal Shock

In the precursor shock case, the pressure pulse has a slower rise to peak and a more irregular decay than that exhibited by the ideal shock (Figure C.2).
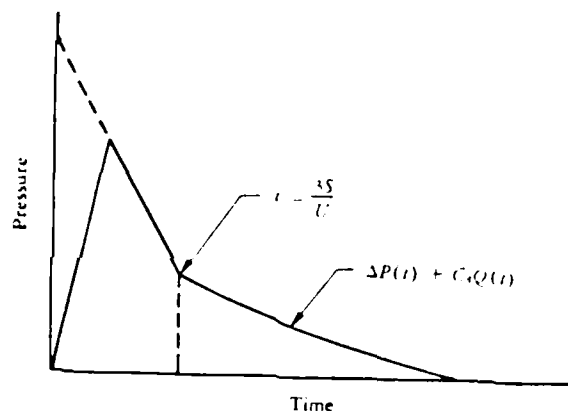
Figure C.2 Slow or Finite Rise-Time Shock

For certain diffraction type targets such slow rising pressures can reduce the damage potential. For drag type targets the damage may actually increase because higher dynamic pressures develop. The pressure histories for the 100 psi overpressure ideal shock and precursor shock were calculated to have the form illustrated below (Figure C.3)
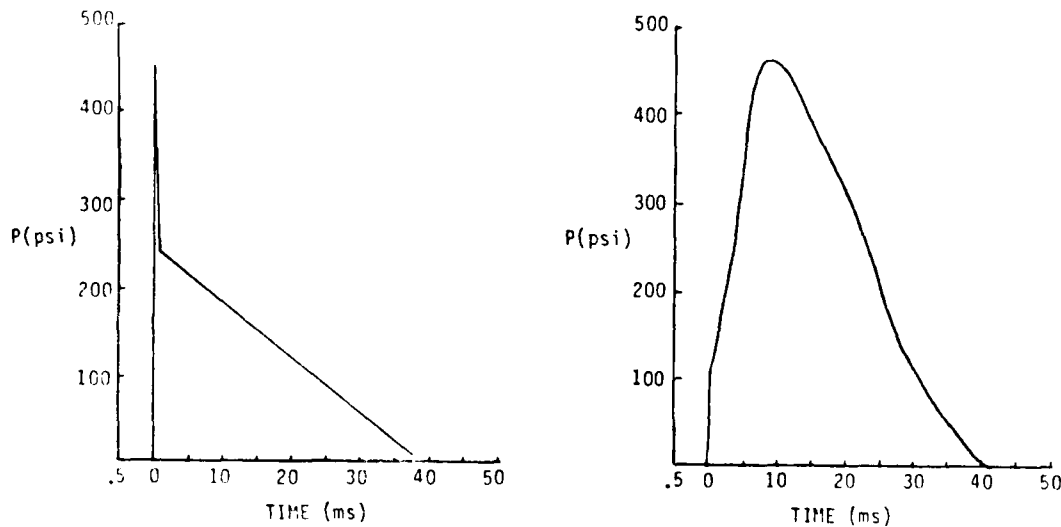
Figure C.3 Front-Face Pressure Versus Time

In the present analysis, the probe stings and rake blades were analyzed separately. In each case it was determined whether the component responded to diffraction loads, drag loads, or both, and then the stresses and deflections were calculated.

The dynamic response of the probe stings and rake blades to blast loading was approximated by an undamped single degree of freedom system subjected to a transient exciting force. Figure C.4 represents response spectra of such undamped oscillators for the excitations used to characterize the blast loads. In these figures, the ratio t_1/τ is the ratio of the characteristic time of the exciting force divided by the natural period of the oscillator. The term $(xk/F_0)_{max}$ is a nondimensional number which is a measure of the dynamic effect over that of a statically applied load.
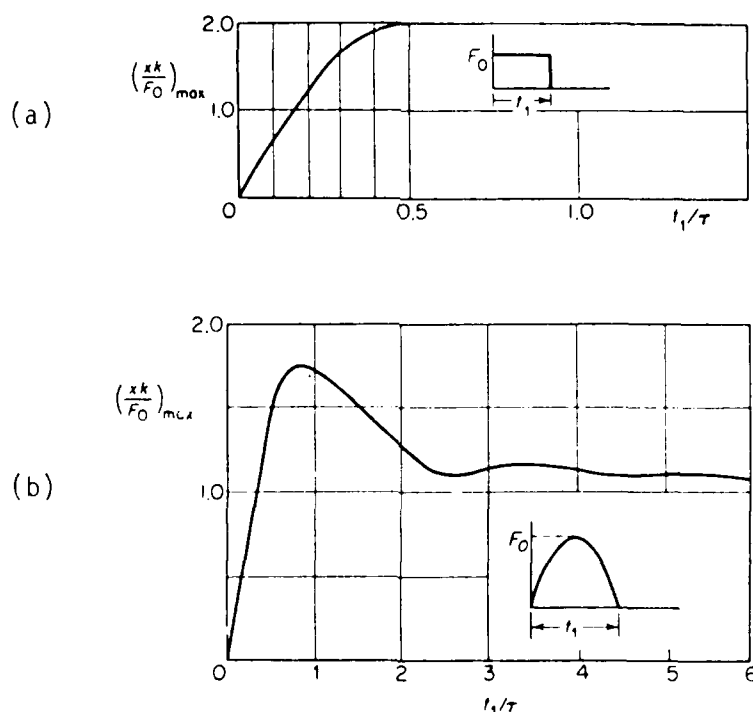
Figure C.4 Response Spectra of Representative Excitations

The characteristic time of the reflected pressure shock was determined by the fact that the reflected pressure shock is reduced to the stagnation pressure at a time after shock arrival approximately equal to $3S/U$ where S equals the height or half width of the structure (whichever is less) and U is the shock speed. For 100 psi overpressures acting on the measurement station, this time is on the order of

C-3

$$t_1 = 1 \times 10^{-4} \text{ sec} \qquad\qquad (C.1)$$

Thus, the initial pulse of the ideal shock load was modeled by Figure C.4(a)

The "tail" of the ideal shock load and the precursor shock have the same characteristic time

$$t_1 = 4 \times 10^{-2} \text{ sec} \qquad\qquad (C.2)$$

Ths loading was modeled by Figure C3.4(a) if $\tau \sim t_1$, or by Figure C.4(b) if $\tau \gg t_1$ or $\tau \ll t_1$. In general, if the component was found to respond to the blast load the dynamic effect was automatically assumed to be an order of 2 greater than the effect due to a statically applied load in order to be on the safe side.

PROBE STINGS

Preliminary Sting Design Considerations

The advantages of using a linearly tapered sting as opposed to a uniform diameter sting are illustrated as follows. The tip deflections and tip angles of a tapered cantilever beam relative to a uniform cantilever beam of I_a (Figure C.5) are given for the case of an end load by

$$y_a' = .354 \ y_a \tag{C.3}$$

$$\theta_a' = .402 \ \theta_a \tag{C.4}$$

and for a distributed load by

$$y_a = .328 \ y_a \tag{C.5}$$

$$\theta_a = .354 \ \theta_a \tag{C.6}$$

Therefore, tapering the beam provides more than a factor of 2 decrease in the tip deflection and angle. In addition, this removes stress raisors and reduces the maximum bending stress $\sigma_{max} = Mc/I$ at the base.
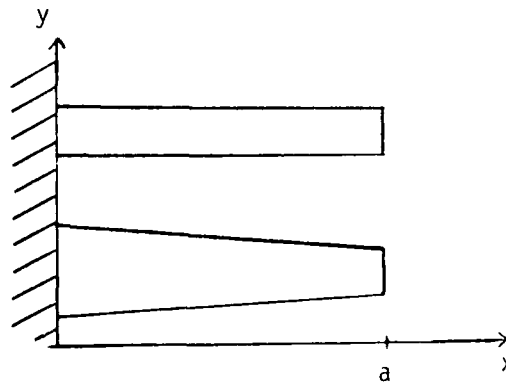
Figure C.5 Tapered Sting

Therefore, the sting will be designed with a linear taper from an outer diameter of 3/4" at the tip to an outer diameter of 1" at the base.

The need for a symmetric noise piece is illustrated as follows. If the probe has a knife edge, it is necessary to look at the aerodynamic tip lift due to the dynamic pressure occurring in ideal shock. This lift will cause a normal force at the tip given by

$$F_N = 4q \; C_D \; A = 500 \text{ lbs.} \tag{C.7}$$

Using flexure formula, the maximum bending moment due to this force is

$$M_b = F_N \ell = 500 \text{ lb} \times 8 \text{ in} = 4,000 \text{ in lb} \tag{C.8}$$

which results in a fiber stress in the sting given by

$$\sigma_{max} = \frac{Mc}{I} = \frac{(4,000 \text{ in lb}) \; (.5 \text{ in})}{.046 \text{ in}^4} = 4.3 \times 10^4 \text{ lb/in}^2 \tag{C.9}$$

This is unacceptable, since the yield strength of steel is 33×10^3 lb/in^2. This points out the need for a symetric nose piece.

Elastic Stability

The elastic stability of the stings was investigated by finding the critical buckling load. As a conservative estimate, a uniform beam with the tip outer diameter was used rather than the tapered beam. The relevant parameters are then

$$1/2\text{" I.D. steel tube} \tag{C.10}$$

$$3/4\text{" O.D.} \tag{C.11}$$

$$I = \left(\frac{\pi}{4}\right)\left(R_o^4 - R_1^4\right) = \left(\frac{\pi}{4}\right)\left(.375^4 - .25^4\right) = 1.24 \times 10^{-2} \text{ in}^4 \tag{C.12}$$

$$A = \pi\left(R_o^2 - R_1^2\right) = \pi\left(.375^2 - .25^2\right) = 2.45 \times 10^{-1} \text{ in}^2 \tag{C.13}$$

$$E = 30 \times 10^6 \text{ lb/in}^2 \tag{C.14}$$

$$k_1 = 0.25 \tag{C.15}$$

which, when used in the critical load formula

$$P_1' = K_1 \frac{\pi^2 E_1 I_1}{\ell^2} \tag{C.16}$$

$$P_1' = 0.25 \frac{\pi^2 \left(30 \times 10^6 \text{ lb/in}^2\right)\left(1.25 \times 10^{-2} \text{ in}^4\right)}{(8 \text{ in})^2} \tag{C.17}$$

yield

$$P_1' = 5.8 \times 10^4 \text{ lbs} \tag{C.18}$$

Therefore, each sting could support 5.8×10^4 lbs of static purely axial loading without buckling.

Natural Period of the Stings

The transverse and axial natural periods of the sting were found by modeling it as a uniform cantilever beam of annular cross section with a weight at the tip. The natural period of the tapered beam (Figure C.5) was assumed to lie between that of the uniform beam with the tips cross-sectional area A_a and moment of inertia I_a, and that of a beam with the base crosssectional area A_b and moments of inertia I_b.

The relevant properties for the sting models of the two different diameter beams were found to be

$$@ \text{ a)} \quad r_a = .75" \qquad\qquad @ \text{ b)} \quad r_b = 1"$$

$E = 30 \times 10^6 \text{ lb/in}^2$	$E = 30 \times 10^6 \text{ lb/in}^2$	(C.19)
$I_a = .0125 \text{ in}^4$	$I_b = .035 \text{ in}^4$	(C.20)
$A_a = .245 \text{ in}^2$	$A_b = .59 \text{ in}^3$	(C.21)
$\omega_a = 6.9 \times 10^{-2} \text{ lb/in}$	$\omega_b = .17 \text{ lb/in}$	(C.22)
$g = 386 \text{ in/s}^2$	$g = 386 \text{ in/s}^2$	(C.23)

The tip weight was approximated as the weight of half of a steel cube with .75 in sides, giving $W = 9.5 \times 10^{-2}$ lb.

The transverse natural frequency of a uniform cantilever with a tip weight and distributed weight is given by

$$f_1 = \frac{1.732}{2\pi} \quad \frac{EIg}{W\ell^3 + .236 \, \omega\ell^4} \tag{C.24}$$

which gives the transverse natural frequencies of the two beams as

$$f_a \sim 310 \text{ Hz} \qquad\qquad f_b \sim 435 \text{ Hz} \tag{C.25}$$

Since the response to fast risetime transient excitation is the important property, the estimate will be weighted toward the higher frequency, and considered to be

$$f_n \sim 400 \text{ Hz (transverse excitation)} \tag{C.26}$$

The axial natural frequency is determined by

$$f_1 = \frac{1}{2\pi} \sqrt{\frac{AEg}{W\ell + \omega\ell^2/3}} \tag{C.27}$$

which gives the axial natural frequency of the two beam models as

$$f_a = 5,700 \text{ Hz} \qquad f_b = 6,300 \text{ Hz} \tag{C.28}$$

so the axial natural frequency will be considered to be

$$f_n \sim 6,000 \text{ Hz} \quad \text{(axial excitation)} \tag{C.29}$$

Thus, the natural periods for the axial and transverse vibrations of the tapered sting are taken to be

$$\tau_{axial} = 1.7 \times 10^{-4} \text{ s} \tag{C.30}$$

$$\tau_{transverse} = 2.5 \times 10^{-3} \text{ s} \tag{C.31}$$

Sting Stresses, Tip Deflections and Tip Angle

The ideal shock diffraction load (P_R) has the characteristic time

$$\tau_1 = 1 \times 10^{-4} \text{ s} \tag{C.32}$$

C-9

and since

$$t_1/\tau_{trans} = \frac{1 \times 10^{-4} \text{ s}}{2.5 \times 10^{-3} \text{ s}} = 0.04 \qquad \text{(C.33)}$$

there will be essentially no transverse response, but since

$$\tau_1/\tau_{axial} = \frac{1 \times 10^{-4} \text{ s}}{1.7 \times 10^{-4} \text{ s}} = 0.6 \qquad \text{(C.34)}$$

the axial excitation causes a dynamic response that is approximately twice as great as the static response. The reflected pressure will cause an axial transient loading of

$$F_{axial} = P_{ref} A_S \cos 45 + P_{ref} A_S \cos 45 \qquad \text{(C.35)}$$

$$P_{refl} = 450 \text{ psi} \qquad \text{(C.36)}$$

$$A_S = (.75) \left(\frac{.75 \sqrt{2}}{2}\right) = .4 \text{ in}^2 \qquad \text{(C.37)}$$

$$F_{axial} = 255 \text{ lb} \qquad \text{(C.38)}$$

which will result in tension and compression stress waves with a maximum

$$\sigma = 2\sigma_{static} = 2 F_{axial}/A_{cross\ sectional} = 2 = 2{,}077 \text{ lb/in}^2 \qquad \text{(C.39)}$$

This is acceptable, since the yield strength of steel is 33×10^3 lb/in^2.

The ideal shock lift and drag loads are characterized by

$$t_1/\tau_{trans} = \frac{4 \times 10^{-2} \text{ s}}{2.5 \times 10^{-2} \text{ s}} = 16 \tag{C.40}$$

$$t_1/\tau_{axial} = \frac{4 \times 10^{-2} \text{ s}}{1.7 \times 10^{-4} \text{ s}} = 400 \tag{C.41}$$

Therefore, both the axial and transverse excitation must be examined.

The transverse tip load due to aerodynamic lift should be negligible for a symmetric nose piece since the angle of attack is zero.

The axial loading due to aerodynamic drag will be

$$F_{axial} = \Sigma F_x = 4 \, q \, C_D \, A \tag{C.42}$$

where

$$C_D = 1.5 \tag{C.43}$$

$$A_F = (.75 \text{ in})^2 = .56 \text{ in}^2 \tag{C.44}$$

$$q = 120 \text{ psi} \tag{C.45}$$

$$F_{axial} = 403 \text{ lb} \tag{C.46}$$

which will cause a maximum stress in the sting of

$$\sigma = 2\sigma_{static} = 3,291 \text{ lb/in} \tag{C.47}$$

which is acceptably less than the 33×10^{-3} lb/in^2 yield strength of steel.

The precursor drag and lift loading, as illustrated below, will cause flexure of the sting. This flexure is due to the combination of both axial and transverse loading on the sting. The transverse loading, using the $\cos^2$ law, is found to be

$$f_n = \frac{F}{in} = 4 \ q \ A/\ell \ C_D \ \cos^2\theta \qquad (C.48)$$

$$q = 120 \ psi \qquad (C.49)$$

$$A/\ell = .75 \ in^2/in \qquad (C.50)$$

$$C_D = 1.5 \qquad (C.51)$$

$$\theta = 70° \qquad (C.52)$$

$$f_n = \ = 54 \ lbs/in \qquad (C.53)$$

The axial loading, again using the $\cos^2$ law, is found to be

$$F = 4 \ q \ A_F \ C_D \ \cos^2\theta \qquad (C.54)$$

$$\theta = 20° \qquad (C.55)$$

$$A_F = (.75 \ in)^2 = .56 \ in^2 \qquad (C.56)$$

$$F = 360 \ lb \qquad (C.57)$$

This combined loading causes a tip deflection y_a and a tip angle θ_a in a uniform cantilever given by

$$y_a = \frac{f_n}{K^2 F} \left(1 + K\ell \ \tan K\ell - \frac{K^2\ell^2}{2} - \frac{1}{\cos K\ell} \right) \qquad (C.58)$$

$$\theta_a = \frac{f_n}{KF} \left(\frac{K\ell}{\tan K\ell} - \tan K\ell \right) \qquad (C.59)$$

where $\quad K = \sqrt{F/EI} \qquad (C.60)$

Therefore,

$$y_a = 7.7 \times 10^{-2} \text{ in} \qquad\qquad (C.61)$$

$$\theta_a = 1.3 \times 10^{-2} \text{ rad} = 7.3 \times 10^{-1} \text{ deg} \qquad\qquad (C.62)$$

The tip deflection and angle of a tapered beam, as previously discussed, are reduced relative to those of a uniform beam of the smaller diameter. Thus

$$y_a = .328 \ y_a \text{ (uniform)} \qquad\qquad (C.63)$$

$$\theta_a = .354 \ \theta_a \text{ (uniform)} \qquad\qquad (C.64)$$

and for a slowly applied load

$$y_a = 2.5 \times 10^{-2} \text{ in} \qquad\qquad (C.65)$$

$$\theta_a = 4.6 \times 10^{-3} \text{ rad} = 2.6 \times 10^{-1} \text{ deg} \qquad\qquad (C.66)$$

For a suddenly applied load these will be increased by a factor of 2, and the tip deflection and angle will be

$$y_a = 5 \times 10^{-2} \text{ in} \qquad\qquad (C.67)$$

$$\theta_a = 5.3 \times 10^{-1} \text{ degress} \qquad\qquad (C.68)$$

Effects of Tip Motion Due to Blast Loading

The effect of tip bending in the plane of the light path is illustrated by the following figure. It is evident from this figure that the worst case occurs when either both mirrors tilt "in", or both mirrors tilt "out" relative to the plane of the light path (in other words, if both stings bend towards each other or apart from each other). If both stings bend equally in this manner, the light reflected off the second mirror is deflected by an angle θ_F equal to 4 times the tip angle. When both stings bend in the same direction the angular deflections of the mirrors tend to cancel each other.

Mirror at
Sting Tip

Mirror at
Sting Tip

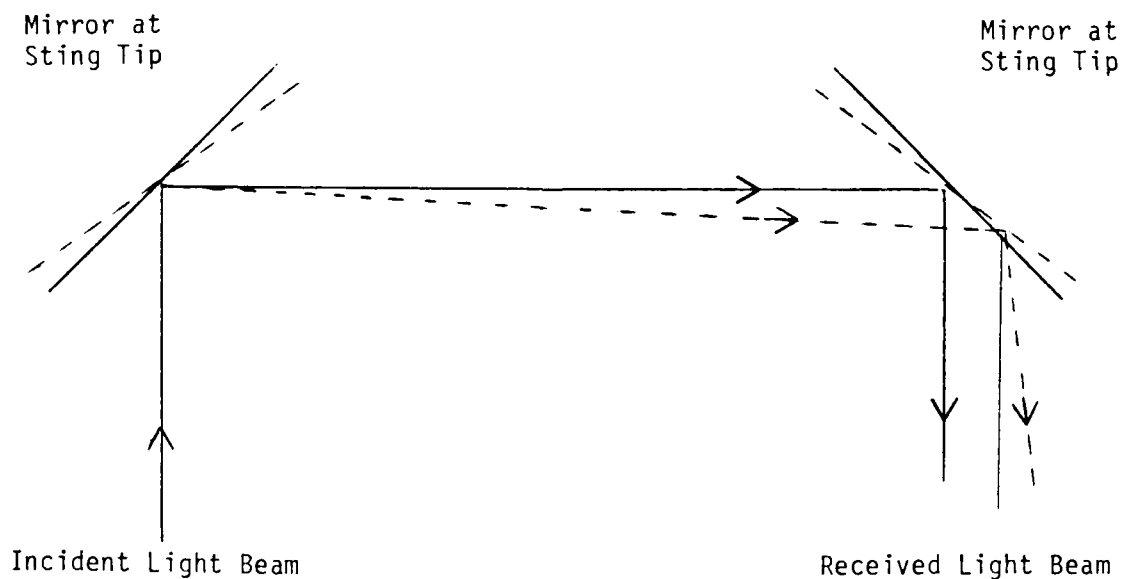Incident Light Beam

Received Light Beam

Figure C.6   Effect of Tip Bending in the Light Path Plane.

A different situation holds for bending out of the plane of the light path. The mirror plane is at 45° to the plane which bends, so if the probe tip bends up at an angle θ_1, the light beam will deflect θ_1 down in the vertical plane normal to the sting. If the other probe tip also moves an angle θ_1, the end result will be to preserve the downward deflection of the beam by θ_1 as it reflects off the second mirror, as shown.

Using the tip deflections and angles calculated in the previous section, the worst case effects of the precursor blast loading on the light path can be found. The uniform drag load from below causes both stings to bend upward, deflecting the beam downwards by .53 degrees across the interrogation path. This will cause a 4.6×10^{-2} cm deflection at the second mirror. The second mirror preserves the $\theta = 0.53$ declination angle, so the beam will be deflected downwards by an additional 0.19 cm as it travels down the receiving sting. When the upward deflection of the tip is taken into account, as illustrated, this results in a .11 cm deflection at the lens.
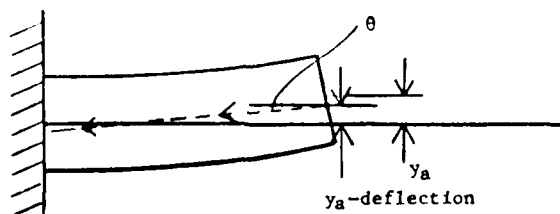

Figure C.7 Effect of Tip Bending Out of
the Light Path Plane.

This deflection can easily be accomodated by an aperture that is 1.5 mm smaller in diameter than the beam diameter at the lens.

In addition to the deflection of the light, the effect of off axis light passing through the lens is to shift the focal point by a distance

$$S = f \tan\theta \qquad\qquad (C.69)$$

where f is the focal length of the collector lens.

Thus, with a 20 mm focal length lens, the maximum calculated tip motion would cause the focused light to move .019 cm down the face of the receiving fiber. This movement can be accomodated by a receiving fiber that is either much larger than the focused spot (so that this movement does not place any of the spot off the fiber face) or much smaller than the spot size (so that this movement does not cause the edge of the spot to cross the fiber face). From system power considerations, the larger fiber is more desirable.

In summary, the deflections of the sting due to precursor blast loads (the worst case) can be accomodated without appreciable signal degradation if the aperture on the receiving optics, and the receiving fiber are sized as previously described. This does not represent a significant departure from the probe configuration used in the laboratory tests. Thus, based on this simplified analysis, the sting sizing is adequate for precursor blast loads.

RAKE BLADES

Loading

The transverse natural period of the rake blade about its minor axis is $\tau = 6.0 \times 10^{-4}$ s, so it will respond weakly to the initial shock, and strongly to the dynamic pressure loading in the direction of the flow. The transverse natural period of the rake blade about its major axis was calculated as

$$\tau = 3.5 \times 10^{-3} \text{ sec} \qquad (C.70)$$

Therefore, its response to shock, as determined by

$$\frac{t_1}{\tau} = \frac{1 \times 10^{-4} \text{ s}}{3.5 \times 10^{-3} \text{ s}} = 2.9 \times 10^{-2} \qquad (C.71)$$

is negligible. Its response to the dynamic pressure loading, characterized by

$$\frac{t_1}{\tau} = \frac{4 \times 10^{-2} \text{ s}}{3.5 \times 10^{-3} \text{ s}} = 11 \qquad (C.72)$$

will be significant.

First, looking at the flexure and stress due to loading in the direction of the flow, the maximum load on the frontal area of the rake blade occurs in the precursor shock, and has a value

$$F = 2P_r \, A_s \, \sin(\alpha) + \Delta p \, A_F + C_D A_F \, q \qquad (C.73)$$

where

$$P_r = 450 \text{ psi} \qquad (C.74)$$
$$A_F = 26 \text{ in}^2 \qquad (C.75)$$
$$q = 120 \text{ psi} \qquad (C.76)$$
$$\Delta p = 100 \text{ psi} \qquad (C.77)$$
$$A_s = 26 \text{ in} \qquad (C.78)$$
$$\alpha = 30° \qquad (C.79)$$
$$C_D = 2 \qquad (C.80)$$

$$F = 2.2 \times 10^4 \text{ lbs} \tag{C.81}$$

The distributed load on the front of the blade is

$$f = \frac{2.2 \times 10^4 \text{ lbs}}{13 \text{ in}} = 1.7 \times 10^3 \text{ lb/in} \tag{C.82}$$

If a worst case is assumed, in which this distributed load continues to the blade base, the top of the rake blade will deflect backwards by

$$y_a = -\frac{f\ell^4}{8EI} \tag{C.83}$$

$$y_a = \frac{(1.7 \times 10^3 \text{ lb/in})(15 \text{ in})^4}{(8)(30 \times 10^6 \text{ lb/in}^2)(236 \text{ in}^4)} = 1.5 \times 10^{-3} \text{ in.} \tag{C.84}$$

If this is increased by a factor of 2 because of sudden loading, the deflection will be

$$y_a = 3.0 \times 10^{-3} \text{ in.} \tag{C.85}$$

which is considered negligible.

The maximum fiber stress occurs at the front edge of the blade, and is given by

$$\sigma = \frac{Mc}{I} = \frac{f\ell^2}{2}\frac{c}{I} \tag{C.86}$$

$$\sigma = \frac{(1.7 \times 10^3 \text{ lb/in})(15 \text{ in})^2}{2}\frac{(6.4 \text{ in})}{(236 \text{ in}^4)} = 5.2 \times 10^3 \text{ lb/in}^2 \tag{C.87}$$

If this is increased by a factor of 2 due to the dynamic loading, the maximum tensile stress will be $1.1 \times 10^4 \text{ lb/in}^2$, which is sufficiently less than steels yield strength in tension of $3.3 \times 10^4 \text{ lb/in}^2$.

Next, the forces developed on the sides of the blade will be investigated. First, because of the knife edge front face a lift force will develop normal to the side of the blades
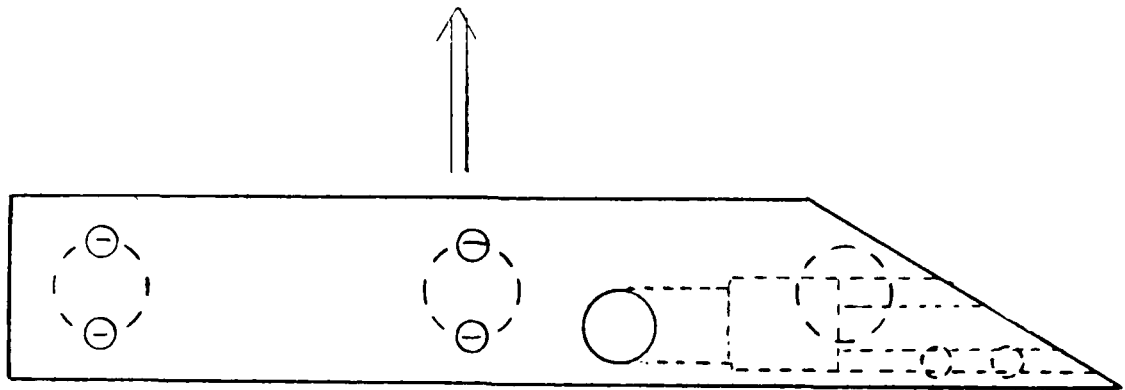
Figure C.8 Blade Rake Side Loading

given by

$$F = 4 q C_D A \qquad (C.88)$$

$$q = 120 \text{ psi} \qquad (C.89)$$

$$C_D = 1.5 \qquad (C.90)$$

$$A = 2 \text{ in} \times 15 \text{ in} = 30 \text{ in}^2 \qquad (C.91)$$

$$F = 2.2 \times 10^4 \text{ lbs} \qquad (C.92)$$

the distributed load on the side of the blade is then

$$f = \frac{2.2 \times 10^4 \text{ lbs}}{13 \text{ in}} = 1.7 \times 10^{-3} \text{ lbs/in} \qquad (C.93)$$

If a worst case is assumed in which the sand bed is eroded and this force acts on the entire blade side the deflection would be

$$z = \frac{-f\ell^4}{8EI} \qquad\qquad (C.94)$$

$$z = \frac{(2.2 \times 10^4 \text{ lb/in}) (15 \text{ in})^4}{(8) (30 \times 10^6 \text{ lb/in}^2) (7.1 \text{ in}^4)} = 0.65 \text{ inches} \qquad (C.95)$$

which is unacceptable. The situation can be rectified by bolting cross members between the tops of the blades. These cross members will need to support half the total load on the blade sides, as illustrated below,
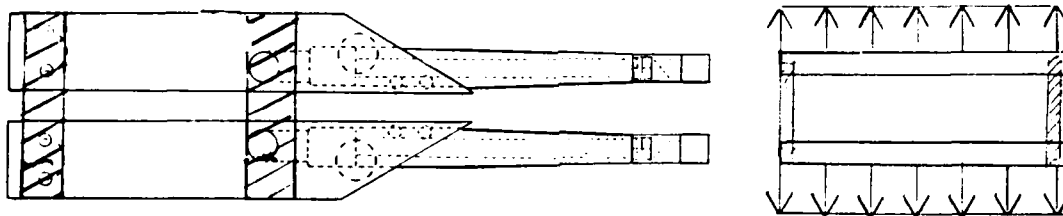
Figure C.9 Connected Blade Rakes

or $F = 1.1 \times 10^4$ lbs. Since the yield strength of steel intension is 3.3×10^4 lb/in^2, the cross members must have a cross sectional rea of at least .33 in^2. A safety factor of three puts the requirement at 1 in^2, which can easily be accomplished with two 1/2 inch by 1 inch bars. The shear on the cross member bolts will be 5.5×10^3 lbs per cross member, which can be accomodated by two 5/8" diameter bolts.

As a conservative estimate, if the precursor flow strikes rake blade at 10° off axis, a force normal to the side of the blade will develop, given by

$$F/R = 4 \, q \, C_L \, A \qquad\qquad (C.96)$$

$$q_{max} = 120 \text{ psi} \qquad\qquad (C.97)$$

$$C_L \sim 0.6 \qquad\qquad (C.98)$$

$$A = 156 \text{ in}^2 \qquad\qquad (C.99)$$

$$F = 4 \ (120 \ psi) \ (0.6) \ (156 \ in^2) \doteq 4.5 \times 10^5 \ lbs \qquad (C.100)$$

The distributed load on the side of the blades is then

$$f = \frac{4.5 \times 10^5 \ lbs}{13 \ in} = 3.5 \times 10^3 \ lb/in \qquad (C.101)$$

If a worst case is assumed in which this distributed load continues to the blade base, the static tip deflection is given by

$$y_a = \frac{-f \ \ell^4}{8 \ EI} \qquad (C.102)$$

$$y_a = \frac{(3.5 \times 10^3 \ lb/in) \ (15 \ in)^4}{(8)(30 \times 10^6 \ lb/in^2)(7.1 \ in^4)} = 1.0 \times 10^{-1} \ in \qquad (C.103)$$

With a dynamic factor of 2; the top of the blade will move $y_a = 2.0 \times 10^{-1}$ inches.

This deflection is reduced by the cross members at the top of the blades. The effect of this modification can be approximated as follows. The second blade is "shaded" by the first blade, as illustrated.
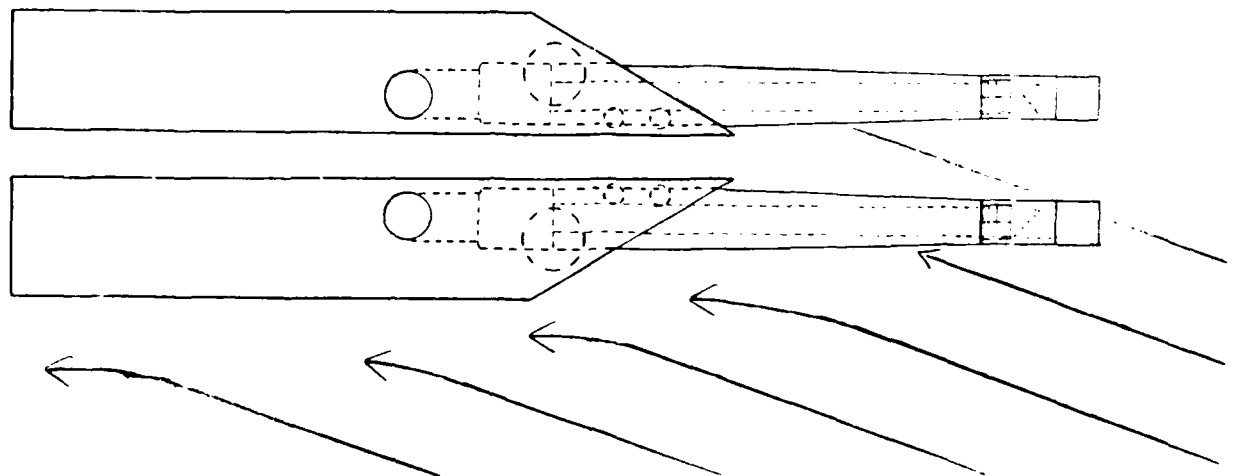
Figure C.10 Shading of One Blade by the Other

so it will be assumed that no aerodynamic forces act on it. When the top of the first blade moves y_a, the second blade resists this with a force

$$F = K\,y_a \qquad \text{where } K = \frac{3EI}{\ell^3} \tag{C.104}$$

$$K = \frac{(3)(30 \times 10^6 \text{ lb/in}^2)(7.1 \text{ in}^4)}{(15 \text{ in})^3} = (1.9 \times 10^5 \text{ lb/in}) \tag{C.105}$$

The situation is then modeled (as shown in Figure C.11) by
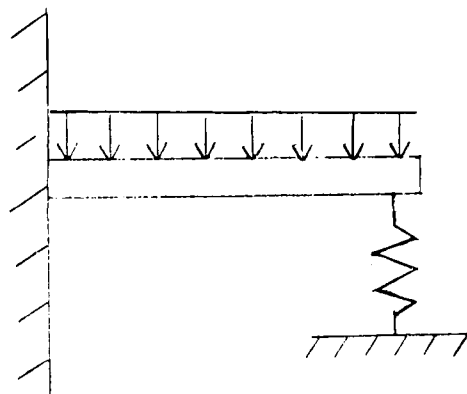
Figure C.11 Blade Interaction

using the principle of superposition, the deflection due to the distributed load

$$y_a = \frac{-f_a\,\ell^4}{8EI} \tag{C.106}$$

and the deflection due to the restoring action of the second blade

$$y_a = \frac{+W\,\ell^3}{3EI}\;; \quad W = F = -Ky_a \tag{C.107}$$

combine to give a total deflection of

$$y_a = - \frac{K y \ell^3}{3EI} - \frac{f \ell^4}{8EI} \; . \tag{C.108}$$

Solving for y_a

$$y_a = \left[- \frac{f_a \ell^4}{8EI} \right] / \left[1 + \frac{K \ell^3}{3EI} \right] \tag{C.109}$$

$$y_a = \frac{1.0 \times 10^{-1}}{1 + 1.004} = .05 \text{ inches} \tag{C.110}$$

If the dynamic factor of 2 is included

$$y_a = 0.10 \text{ inches} \tag{C.111}$$

Thus, the cross member reduces the deflection bu a factor of 2. In reality, a cross member would have even more effect since it would act to form a frame, and thus also introduce restoring moments at the blade tips.

BOLT SIZING

Bolt Shear for Precursor Shock with Dust Loading

The shear on the bolts holding the blades to the base plate is found as follows. The total axial force on the rake was calculated in the discussion of rake blade loading as

$$F = 2.5 \times 10^4 \text{ lbs} \tag{C.112}$$

and the lift force on the blade sides was found to be

$$F = 2.2 \times 104 \text{ lbs} \tag{C.113}$$

and thus the shear at blade base is

$$V = 3.3 \times 10^4 \text{ lbs} \tag{C.114}$$

The present design uses (3) 1-1/4" bolts and (2) 3/8" bolts to secure the rake blade to the base plate. The maximum allowable shear per bolt is given by the bolt area x 10 Kips so the maximum allowable shear with this configuration is

$$V = (3) \ (9.94 \times 10^3 \text{ lbs}) + (2) \ (1.1 \times 10^3 \text{ lbs}) = 3.2 \times 10^4 \text{ lbs} \tag{C.115}$$

This provides 33% factor of safety for a slowly applied load, but does not include the factor of 2 for sudden loading. This factor of 2 can be obtained by adding a "backbar" with (2) 1-1/4" bolts per blade to bring the total number of 1-1/4" bolts per blade to (5). Thus, the maximum allowable shear is increased to

$$V = (5) \ (9.94 \times 10^3 \text{ lbs}) + (2) \ (1.1 \times 10^3 \text{ lbs}) = 5.2 \times 10^4 \text{ lbs} \tag{C.116}$$

which provides the factor of 2 necessary for sudden loading.

BOLT TENSILE STRESS

The tensile stress on the bolts that hold the base plate to the floor (or the concrete pad_ can be found as follows. If the axial force on the blades found in the previous section is considered a distributed load,

$$f = \frac{2.4 \times 10^4 \text{ lbs}}{13 \text{ in}} = 1.8 \times 10^3 \text{ lb/in} \tag{C.117}$$

and as a worst case this distributed load acts over the entire blade, the moment is

$$M = \frac{f \ell^2}{2} = (1.8 \times 10^3 \text{ lb/in}) (15 \text{ in})^2/2 = 2.1 \times 10^5 \text{ lb/in} \tag{C.118}$$

The maximum tensile fiber stress in the rake blade occurs at the leading edge of the rake base, and has a magnitude

$$\sigma_{max} = \frac{Mc}{I} \tag{C.119}$$

$$\sigma = \frac{(2.1 \times 10^5 \text{ lb in}) (6.4 \text{ in})}{(236 \text{ in}^4)} \cong 6.0 \times 10^3 \text{ lb/in}^2 \tag{C.120}$$

which is approximately a factor of 5 below steel's yield strength of 3.3×10^4 lb/in^2 in tension.

The tensile stress in the base plate bolts can be approximated by the taking the moment due to the actual force on the rake times the lever arm of the base At a point 7 in. forward of the rake neutral axis the upward force is

$$F = (6.0 \times 10^3 \text{ lb} \cdot \text{in})/(7 \text{ in}) = 8.6 \times 10^2 \text{ lbs} \tag{C.121}$$

Thus, if only (1) 1-1/4" steel bolt (.994 in^2) per blade is placed at this point, the axial stress is

$$\sigma = \frac{8.6 \times 10^2 \text{ lbs}}{0.994 \text{ in}^2} = 8.7 \times 10^3 \text{ lb/in}^2 \qquad \text{(C.122)}$$

which is well below the yield stress of 33×10^3 lbs/in^2 for steel.

STRESSES IN THE OPTICAL WINDOW

The stresses in the windows are approximated by the stresses in a simply supported uniform circular plate with a uniformly distributed load, i.e.,

$$\text{Max } \sigma = \frac{6M_c}{t^2} \tag{C.123}$$

where   t is the thickness (~ .125 inches)

Mc is moment at the center given by

$$M = \frac{q\,a^2}{16}\,(3+v) \tag{C.124}$$

where   q is the uniformly distributed load (100 psi)

a is the diameter (~ .6 in.)

v is Poisson's ratio (~ 0.28)

$$M = \frac{(100\text{ psi})(.36\text{ in}^2)}{16}\,(3.28) = 7.4\,\frac{\text{in-lb}}{\text{in}} \tag{C.125}$$

and the maximum bending stress is

$$\text{Max } \sigma = \frac{(6)\,7.4\text{ in-lb/in}}{(.125\text{ in})^2} = 2{,}834\text{ psi} \tag{C.126}$$

Since glass has a compressive working strength > 100,000 psi and tensile strength > 25,000 psi, this is considered acceptable.

DISTRIBUTION LIST

DEPARTMENT OF DEFENSE

Asst to the Secretary of Defense, Atomic Energy
    ATTN: Executive Assistant

Commander in Chief, Atlantic
    ATTN: J7

Defense Intelligence Agency
    ATTN: DT-1B
    ATTN: DT-2
    ATTN: RTS-2B

Defense Nuclear Agency
    ATTN: SPAS
    ATTN: STSP
4 cy ATTN: STT1-CA

Defense Technical Info Ctr
12 cy ATTN: DD

Field Command, DNA, Det 2
Lawrence Livermore National Lab
    ATTN: FC-1

Field Command
Defense Nuclear Agency
    ATTN: FCPR
    ATTN: FCTT, W. Summa
    ATTN: FCTXE

Joint Chiefs of Staff
    ATTN: GD10, J-5 Nuc & Chem Div

Joint Strat Tgt Planning Staff
    ATTN: JLK, DNA Rep
    ATTN: JLKS
    ATTN: JPPFM

Under Secy of Def for Rsch & Engrg
    ATTN: Strat & Space Sys (OS)
    ATTN: Strat & Theater Nuc For, B. Stephan

DEPARTMENT OF THE ARMY

BMD Advanced Technology Center
    ATTN: ATC-D, Watts
2 cy ATTN: ATC-R, Andrews

BMD Program Office
    ATTN: DACS-BM/Technology Div

Dep Ch of Staff for Ops & Plans
    ATTN: DAMO-NCZ

Dep Ch of Staff for Rsch Dev & Acq
    ATTN: DAMA-CSS-N

Harry Diamond Laboratories
    ATTN: DELHD-NW-RH, 22800

US Army Ballistic Research Labs
    ATTN: DRDAR-BL, R. Eichelberger

US Army Material & Mechanics Rsch Ctr
    ATTN: DRXMR-HH

DEPARTMENT OF THE ARMY (Continued)

US Army Material Command
    ATTN: DRCDE-D

US Army White Sands Missile Range
    ATTN: STEWS-NR-CF, R. Valencia
    ATTN: STEWS-TE-LD, J. Blaine

USA Missile Command
    ATTN: DRSMI-RH

DEPARTMENT OF THE NAVY

Naval Ordnance Station
    ATTN: J. Miller, Code 5422 I

Naval Research Laboratory
    ATTN: Code 2627, Tech Lib

Naval Sea Systems Command
    ATTN: SEA-0351

Naval Surface Weapons Center
    ATTN: Code K06
2 cy ATTN: Code K82

Ofc of the Deputy Chief of Naval Ops
    ATTN: NOP 654, Strat Eval & Anal Br

Strategic Systems Project Office
    ATTN: NSP-272

DEPARTMENT OF THE AIR FORCE

Air Force Geophysics Laboratory
    ATTN: D. McLeod

Air Force Rocket Propulsion Lab
    ATTN: LKCP

Air Force Wright Aeronautical Lab
    ATTN: LTM
    ATTN: MLBC
    ATTN: MLP

Air Force Systems Command
    ATTN: DLW

Air Force Weapons Laboratory
    ATTN: SUL

Air Force Wright Aeronautical Lab
    ATTN: FIBC
    ATTN: FIMG

Air University Library
    ATTN: AUL-LSE

Ballistic Missile Office
    ATTN: ENMR
    ATTN: ENSN

Deputy Chief of Staff, Rsch, Dev & Acq
    ATTN: AF/RDQI

DEPARTMENT OF THE AIR FORCE (Continued)

Deputy Chief of Staff, Rsch, Dev & Acq
    ATTN: AFRDS, Space Sys & C3 Dir

Foreign Technology Division
    ATTN: SDBG

Strategic Air Command
    ATTN: NRI/STINFO

Strategic Air Command
    ATTN: XPFS

Strategic Air Command
    ATTN: XPQ

161 ARG / izona Ang
2 cy ATTN: Lt Col Sherer

OTHER GOVERNMENT AGENCIES

Central Intelligence Agency
    ATTN: OSWR/NED

NATO

NATO School, SHAPE
    ATTN: US Documents Officer

DEPARTMENT OF ENERGY CONTRACTORS

University of California
Lawrence Livermore National Lab
    ATTN: L-10, H. Kruger
    ATTN: L-8, P. Chrzanowski

Los Alamos National Laboratory
    ATTN: R. Selden

Sandia National Laboratories
    ATTN: D. Rigali
    ATTN: Org 7112, A. Chabai
    ATTN: R. Clem
    ATTN: 0334, J. Struve

DEPARTMENT OF DEFENSE CONTRACTORS

Acurex Corp
    ATTN: C. Nardo
    ATTN: C. Powars
    ATTN: J. Crenshaw
    ATTN: J. Saperstein

Aerojet General Corp
    ATTN: R. Jenkins

Aerospace Corp
    ATTN: D. Platus
    ATTN: W. Portenier

APTEK, Inc
    ATTN: T. Meagher

AVCO Systems Division
    ATTN: A. Pallone
    ATTN: J. Stevens
    ATTN: V. Dicristina
    ATTN: W. Broding

DEPARTMENT OF DEFENSE CONTRACTORS (Continued)

Dynamics Technology, Inc
    2 cy ATTN: M. Petach
    2 cy ATTN: C. Dube
    2 cy ATTN: D. Hove

Fiber Materials, Inc
    ATTN: M. Subilia, Jr.

General Electric Co
    ATTN: A. Garber
    ATTN: B. Maguire
    ATTN: D. Coceano

General Research Corp
    ATTN: R. Parisse
    ATTN: R. Williams

Institute for Defense Analyses
    ATTN: Classified Library

Kaman Sciences Corp
    ATTN: F. Shelton

Kaman Sciences Corp
    ATTN: E. Conrad

Kaman Tempo
    ATTN: DASIAC

Kaman Tempo
    ATTN: DASIAC

Lockheed Missiles & Space Co., Inc
    ATTN: D. Price
    ATTN: G. Chrusciel
    ATTN: J. Lee
    ATTN: P. Schneider

Martin Marietta Corp
    ATTN: L. Kinnaird

McDonnell Douglas Corp
    ATTN: L. Cohen, MS 13-3
    2 cy ATTN: H. Morris
    2 cy ATTN: J. Mardacci

McDonnell Douglas Corp
    ATTN: M. Potter

National Academy of Sciences
    ATTN: Natl Materials Advisory Board

Pacific-Sierra Research Corp
    ATTN: H. Brode, Chairman SAGE

Pan Am World Service, Inc 2
    ATTN: AEDC/Library Doc, TRF

PDA Engineering
    ATTN: J. Dunn
    3 cy ATTN: C. Thacker

Physics International Co
    ATTN: J. Shea

Rand Corp
    ATTN: P. Davis

DEPARTMENT OF DEFENSE CONTRACTORS (Continued)

Rand Corp
    ATTN: B. Bennett

R&D Associates
    ATTN: F. Field
    ATTN: P. Haas
    ATTN: P. Rausch
    ATTN: R. Ross

S-CUBED
    ATTN: G. Gurtman

Science Applications Intl Corp
    ATTN: J. Warner

Science Applications Intl Corp
    ATTN: R. Potts

Science Applications Intl Corp
    ATTN: J. Cockayne
    ATTN: W. Layson

Science Applications Intl Corp
    ATTN: A. Martellucci

Southern Research Institute
    ATTN: C. Pears

Calspan Corp
    ATTN: M. Holden

DEPARTMENT OF DEFENSE CONTRACTORS (Continued)

Space Data Corp
    ATTN: B. Bollermann

Sparta Systems, Inc
    ATTN: D. Landaur

Spectron Development Labs, Inc
    ATTN: T. Lee

SRI International
    ATTN: D. Curran
    ATTN: G. Abrahamson

TRW Electronics & Defense Sector
    ATTN: D. Baer
    ATTN: R. Myer
    ATTN: W. Wood

TRW Electronics & Defense Sector
    ATTN: E. Allen
    ATTN: E. Wong
    ATTN: L. Berger
    ATTN: V. Blankinship
    ATTN: W. Grabowski
    ATTN: W. Polich

Weidlinger Assoc., Consulting Engrg
    ATTN: T. Deevy

END

FILMED

1-86

DTIC